Revision 2

Characterization and potential toxicity of asbestiform erionite from Gawler Downs, New Zealand

Janki Patel[1*], Martin Brook[1], Melanie Kah[1], Ayrton Hamilton[1], Maria Cristina Gamberini[2], Carlotta Zoboli[2], Enrico Mugnaioli[3], Daniele Malferrari[4], Riccardo Fantini[4], Rossella Arletti[4], Alessandro F. Gualtieri[4]

[1]School of Environment, University of Auckland, Private Bag 92019, Auckland 1010, New Zealand
[2]Department of Life Sciences, University of Modena and Reggio Emilia, Via G. Campi 103, 41125, Modena, Italy
[3] Department of Earth Sciences, University of Pisa, Via S. Maria 53, 56126, Pisa, Italy
[4]Department of Chemical and Geological Sciences, University of Modena and Reggio Emilia, Via G. Campi 103, 41125, Modena, Italy

To be submitted to the American Mineralogist

*corresponding author e-mail address: janki.patel@auckland.ac.nz

ABSTRACT

Erionite is the name for a zeolite mineral series originating from diagenesis or hydrothermal alteration of volcanic rocks. The particular erionite 'species' is based on the dominant extra-framework cation, erionite-Ca, erionite-K, or erionite Na. Irrespective of the species, erionite can display a fibrous/asbestiform morphology and has been linked with cases of malignant mesothelioma, a disease typically associated with asbestos exposure. Characterization of new discoveries of erionite is therefore important to assess any potential exposure hazards. This study describes a new asbestiform erionite from vesicles within the Upper Cretaceous Mt. Somers Volcanics Group (MSVG), Canterbury, New Zealand. The erionite is within the Hinds River Dacite, the youngest unit within the MSVG at Gawler Downs, ~100 km west of Christchurch, in the foothills of the Southern Alps. A multi-analytical approach was taken to analyze the sample which included micro-Raman spectroscopy, thermogravimetric analysis, electron microscopy, electron microprobe analysis, and X-ray powder diffraction with the Rietveld method. Results confirmed the mineral as fibrous erionite-K. The chemical composition of the mineral is unique due to the presence of higher levels of Mg. While Fe was also identified, this was due to smectite flakes occurring on the surface of the erionite fibers. According to the World Health Organization (WHO) respirable mineral fiber definition, where length $\geq$ 5 μm, width $\leq$ 3 μm, and aspect ratio (L/w) $\geq$3:1, the Gawler Downs erionite fibers are respirable, while the fibers themselves exceed respirable thickness. In addition to morphology, a value for the potential toxicity model was also computed (2.28 for the Gawler Downs erionite). This is similar to other carcinogenic erionites from Karain, Turkey (2.33), and Nevada, USA (2.28). Taken together,

results indicate Gawler Downs erionite represents an environmental hazard. Nevertheless, further investigation is required to determine potential environmental exposure pathways by which erionite may become airborne and assess the actual environmental risk in the Gawler Downs area.

Key-words: erionite, asbestos, crystal structure, toxicity, carcinogenicity.

INTRODUCTION

Erionite is a widespread natural zeolite (framework type ERI) with ideal chemical formula $K_2(Ca_{0.5},Na)_7[Al_9Si_{27}O_{72}]\cdot 28H_2O$ (Passaglia and Sheppard 2001). The name erionite comes from the Greek εριου = wool because this fibrous zeolite sometimes presents a woolly appearance (Gottardi and Galli 1985). Erionite is included in the ABC–6 family (Gottardi and Galli 1985) and displays a periodic building unit (PerBU) consisting of a hexagonal array of planar 6–membered rings of $(Si,Al)O_4$ tetrahedra (T6–rings) related by pure translations along *a* and *b* (Gualtieri et al. 1998; Baerlocher et al. 2007). Its symmetry is hexagonal with space group $P6_3/mmc$ and unit-cell parameters $a \sim 13.15$ Å, $c \sim 15.05$ Å. In the stacking sequence of erionite, neighboring T6–rings are connected through tilted 4–rings along [001] following the AABAAC… sequence. The framework is characterized by three types of cavities: the cancrinite cage ($[4^6 6^5]$ polyhedra), double 6–ring (D6R) cages (hexagonal prism, $[4^6 6^2]$ polyhedron, formed by two 'A' 6–rings), and columns of erionite cavities ($[4^{12}6^5 8^6]$ polyhedral) between the 'B' or 'C' 6–rings (Staples and Gard 1959; Gottardi and Galli 1985; Armbruster and Gunter 2001; McCusker et al. 2001). Erionite has a large chemical variability with three most abundant

species: erionite-Na, erionite-K, and erionite-Ca (Gualtieri et al. 1998; Passaglia et al. 1998). K^+ cations are located at the center of the cancrinite cages while Na^+, Ca^{+2}, Mg^{2+} and water molecules occupy the erionite cavities and are distributed on sites located on the symmetry axis (Gualtieri et al. 1998). Alberti et al. (1997) found that in the erionite cavities there are three partially occupied positions Ca1, Ca2, Ca3 and each is coordinated with water molecules. One additional cation site was observed at special position (½, 0, 0) by Ballirano et al. (2009) and Giacobbe et al. (2023) in erionite-K and labeled as K2. This site corresponds to the K site found by Schlenker et al. (1977) in dehydrated erionite-Ca and to the Ca4 site found by Gualtieri et al. (1998) in some natural erionite-Ca samples (Ballirano and Cametti 2012; Ballirano et al. 2017).

In nature, erionite occurs in two genetic environments: (i) diagenetic as alteration of vitroclastic rocks (with mean R=[Si+Al]/Si=0.78). In tuffaceous rhyolites and altered tuffs, both hydrologically closed or open systems/autoclave genesis are observed (Gottardi and Galli 1985). For this environment, formations in lacustrine beds and burial diagenesis are also possible genetic mechanisms; (ii) hydrothermal (with mean R= 0.75) in the vugs of altered volcanic rocks such as basalts, andesites, limburgites, and many more (Passaglia et al. 1998; Passaglia and Sheppard 2001).

The crystal habitus of erionite observed in both diagenetic and hydrothermal environments are manifold as evidenced by the countless number of terms used in literature to describe erionite crystals including prismatic, acicular, needles, rods, fibrous, fibers, hair-like, woolly, bundles, radiating clusters (Dogan et al. 2008; Giordani et al. 2017). A simplified classification of the erionite crystal habit is: (a) stocky hexagonal prisms usually terminated with basal pinacoids like the diagenetic erionite crystals from Durkee, Oregon USA (Gottardi and Galli 1985); (b) acicular

hexagonal prisms with regular or irregular basal terminations. A nice example of hydrothermal acicular erionite can be found at the Niigata Prefecture, Japan (Harada et al. 1967); (c) fibrous hexagonal prisms or fiber bundles with regular or irregular basal terminations like the erionite crystals from Oregon USA (Gottardi and Galli 1985), and most of the Turkish (Cappadocia) and American diagenetic erionite samples (Van Gosen et al. 2013); (d) aggregates of stocky/fibrous hexagonal prisms (amygdaloid) like the diagenetic erionite samples from Bowie, Arizona USA (Gottardi and Galli 1985); (e) woolly asbestiform fiber bundles like the flexible hair-like fibers having a width of about 0.1 μm, extremely variable lengths and sometimes curious "brush-like" terminations observed in the erionite samples from Lessini Mounts in Italy (Giordani et al. 2016). It should be noted that erionite intergrowth with offretite (framework type OFF) is very common because of the close similarity of the crystal-structure and crystal-chemical assemblages of these two zeolites. In fact, offretite has an ideal chemical formula of $K_2(Ca_{0.5},Na)_4Mg_2[Al_{10}Si_{26}O_{72}]\cdot 32H_2O$ (Passaglia and Sheppard 2001) and hexagonal symmetry with space group $P\bar{6}m2$ and unit-cell parameters $a \sim 13.30$ Å, $c \sim 7.60$ Å. Passaglia et al. (1998) reported that the two zeolites have well-defined compositional fields and the crystal chemistry of the Mg cation is a major factor in controlling their crystallization.

Erionite can have a fibrous or asbestiform morphology and its exposure has been linked to cases of malignant mesothelioma, a fatal and aggressive cancer (Bariş et al. 1996). Importantly, fibrous/asbestiform erionite appears to be even more carcinogenic than the six regulated asbestos minerals (Wylie 2017). The first health issues regarding erionite exposure and mesothelioma were noted in Cappadocia (Turkey), and more recently, occupational exposure issues have emerged in the USA (Van Gosen et al. 2013). The International Agency for Research on Cancer

106 (IARC) has classified erionite as a Group 1 carcinogen (IARC 1997). Nevertheless, when
107 erionite fibers remain undisturbed in rock and/or soil, they are assumed not to pose a risk to
108 human health. Airborne fibers, however, may be considered toxic if they satisfy the following
109 size requirements set out by the World Health Organization to be considered respirable; length ≥
110 5 μm, width ≤ 3 μm, and aspect ratio (L/w) ≥3:1 (WHO; 1986, 1997).
111 In New Zealand, erionite has been found in surface rock exposures at numerous locations
112 throughout both the North and South Islands, including (from north to south) Kaipara, Auckland,
113 Taupo Volcanic Zone, Banks Peninsula, and the Moeraki coast (Patel et al. 2022). New Zealand
114 is one of a number of high-income countries with an elevated incidence of malignant
115 mesothelioma cases (2.6 per 100,000), thought to result from occupational exposure to airborne
116 asbestos fibers. Thus, understanding the distribution and character of erionite in New Zealand
117 and assessing the potential exposure risk for the population is crucial as residential land
118 development is occurring in some areas where erionite is known to be present (Brook et al.
119 2020). To this aim, a systematic long term study of the mapping and crystal chemical
120 characterization of erionite in New Zealand started in 2020 (Brook et al. 2020; Patel and Brook
121 2021; Patel et al. 2022).
122 In this scenario, our work describes for the first time the crystal chemistry and morphology of
123 an outstanding asbestiform erionite from Gawler Downs, New Zealand to assess if this fiber can
124 represent an environmental hazard. The work takes advantage of a suite of complimentary
125 experimental techniques to comprehensively characterize the sample and predict its potential
126 toxicity and carcinogenicity.
127

SOURCE OF THE SAMPLE AND GEOLOGICAL OVERVIEW

The sample site (GD4a) lies within the Gawler Downs, which are foothills of the Southern Alps, 35 km northwest of Ashburton on New Zealand's South Island (Fig. 1). This is a landscape of downlands, comprising subdued landscapes of undulating smooth hills or broad ridges dissected by steep gullies draining to broad floodplains. Gawler Downs is composed of the erosional and block-faulted remnants of a suite of Late Cretaceous calc-alkaline volcanic rocks, the Mount Somers Volcanics Group (MSVG; Oliver and Keene 1989). These volcanic flows and domes are preserved discontinuously in the eastern foothills of the Southern Alps, northeastwards from the Rangitata River gorge to the Malvern Hills (Fig. 1). This ~18,000 km^2 volcanic center represents the youngest (ca. 99-96 Ma; Van der Meer et al. 2017) known calc-alkaline volcanism in Zealandia during its Paleozoic-Mesozoic Gondwana active margin setting(Oliver and Keene 1989; Tappenden 2003; Van der Meer et al. 2017). Erupted magma volumes are thought to have been similar to the present-day Taupo Volcanic Zone (Tappenden 2003), and MSVG units intruded and overly Torlesse meta-sediments of the Permian to Late Triassic Rakaia Terrane (Smith and Cole 1996). Paleogene to Holocene cover strata are interpreted to overlay most of the MSVG deposits which also continue under the Canterbury Plains and offshore (Field and Browne 1989).

The MSVG can be divided into intermediate/basic (basaltic andesite to dacite) and rhyolitic/ignimbrite rocks, although Oliver and Keene (1989) and Smith and Cole (1996) report much more detailed, and contrasting, stratigraphic nomenclatures. Nevertheless, at the main MSVG occurrence in the Mt Somers area to the north of Gawler Downs (Fig. 1a), the oldest units consist of both massive and bedded rhyolitic tuff, recording the first explosive silicic

150 volcanism at Mt. Somers. Barrossa Andesite crops out over ~2 km^2 to the north and northwest of
151 Mt. Somers, overlying Surrey Hills Tuff and in some places directly overlying Torlesse
152 greywacke (Smith and Cole 1996). Barrossa Andesite forms lava flows up to 80 m thick, and is
153 overlain by younger ignimbrite, rhyolite and tuffs. Where fresh, the ignimbrite units are a
154 moderately indurated, black, glassy, porphyritic vitrophyre which contains up to 15% lithic
155 fragments. It weathers to a friable, green-grey glassy sand and in extreme situations, to a green
156 bentonite (Smith and Cole 1996). Silica contents decrease stratigraphically upwards towards
157 dacites and andesites, the Hinds River Dacite being the youngest MSVG unit (Oliver and Keene
158 1989; Smith and Cole 1996).

159 At Gawler Downs, the Hinds River Dacite covers most of the area, although outcrop is sparse
160 (Fig. 1b and Fig. 1c), aside from valley floors where the GD4a sample was extracted from, close
161 to Surrey Stream (Fig. 1c). The Hinds River Dacite includes glassy and porphyritic dacite flows
162 and dikes. The dacites are dominated by heavily weathered, often rubbly and amygdaloidal flows
163 (Tappenden 2003), and the basal beds of the dacite show considerable hydrothermal alteration as
164 a result of the hot dacite lava having flowed over the wet, bedded tuff. The tuff present at Gawler
165 Downs underlies the Hinds River Dacite and outcrops to the east of the Gawler Downs trig point,
166 as pale green and pink laminated fine siltstone. The mineral assemblage consists of plagioclase,
167 sanidine, quartz, biotite, garnet and opaque minerals (ilmenite), which indicates a relationship
168 between the tuff and the overlying volcanic units (Tappenden 2003). A small outcrop of tuff
169 underlying the Hinds River Dacite also occurs near the headwaters of Surrey Stream, south-west
170 of the Gawler Downs trig station (Oliver 1977; Fig. 1c).

The site of GD4a occurrence consisted of a road-cutting up to 2 m in height and 100 m across (Fig. 2a), the dacite flows and tuff layers within the outcrop had been hydrothermally altered and infilled with silica (agate, chalcedony, opal and quartz), clays and zeolites, as well as silicification and veining (Field and Browne 1989; Oliver and Keene 1989). The rock sampled had a phaneritic texture and was a moderately weathered ash deposit that had a vesicle ~3 cm present and infilled with the fibrous erionite (Fig. 2b). Smaller vesicles up to 5 mm wide were not infilled.

SAMPLING PROCEDURE

The sampling method engaged for collecting the erionite samples involved surveying the volcanic rock for vesicles infilled with a fibrous material. Using a geological hammer, the vesicles found were dislodged from the host rock and placed in a plastic bag, approximately ~400 g of the host rock was also taken. Samples were stored in separate plastic bags to prevent cross contamination and reduce any adverse health effects from fibers becoming airborne and inhaled during transportation to the labs. For analysis, samples of the fibers were prepared by drying and cryo-milling to crush the powder finely. Fibrous bunches were also used for scanning electron microscopy (SEM) as well as homogenized while mixed with acetone to disperse the fibers on carbon tape.

METHODS

The Raman analyses were conducted with a confocal micro-Raman LabRAM HR evolution (Horiba Jobin Yvon, Edison, USA), equipped with a red He-Ne laser at 532 nm (1 μm-size spot),

193 notch filters to eliminate the exciter, detector CCD front illuminated open electrode multi-pin
194 phased, with 1024×256×16 pixels, cooled by a Peltier system. Spectra were recorded in
195 backscattering after focalization in several positions within a small area of the sample (ca.
196 100×100 μm). The maximum laser power employed was 20 mW and the recording time for a
197 good signal-to-noise ratio was 10 s for 50 accumulations. Furthermore, LabSpec6 was used for
198 the spectra elaboration.
199 Thermogravimetric (TGA) measurements were carried out with a Seiko SSC 5200 thermal
200 analyzer coupled with a quadrupole mass spectrometer (ESS, GeneSys Quadstar 422) to detect
201 the volatiles evolved during thermal reactions (MSEGA). Experimental conditions were: heating
202 rate: 20 °C/min; thermal range: 25-850 °C; purging gas: ultrapure helium, flow rate: 100 μL/min.
203 Mass analyses were carried out to detect the possible emission of H_2O, CO_2 and SO_2 as the most
204 likely gaseous compounds resulting from dehydration and/or thermal decomposition of
205 impurities; for this purpose, intensity as a function of temperature was measured for the m/z
206 signals 18, 44 and 64 for H_2O, CO_2 and SO_2, respectively, where m/z is the dimensionless ratio
207 between the mass number and charge of an ion.
208 The morphological observation of the samples was carried out by a Scanning Electron
209 Microscope (SEM) using JSM-6020PLUS/LA (JEOL, Hillsboro, USA) equipped with an Energy
210 Dispersive X-ray (EDX) spectrometer (Oxford INCA-350) and Field Emission Gun Scanning
211 Electron Microscope (FEG-SEM) FEI Nova NanoSEM 450 FEG-SEM. An aliquot of raw
212 sample was fixed on an aluminum stub with double-stick carbon tape and coated with a thin film
213 of carbon (10 nm of thickness), using a Carbon Coater-Balzers CED-010. A series of

representative SEM images were obtained by secondary electron (SE) signal and analysed using ImageJ software.

For the electron microprobe analysis (EMPA), quantitative wavelength dispersion spectrometry (WDS) microanalyses were performed on a few sample aggregates embedded in resin discs of 1 inch and polished at 1 μm. The employed instrument was a JEOL 8200 Super Probe with W hairpin type filament, equipped with five wavelength-dispersive spectrometers. Analyses were performed with atomic number resolution on BSE (Z): less/equal than 0.1 (CuZ), accelerating voltage of 15 kV, detectable wavelength of 0.087 to 9.3 nm, specimen current of 5 nA, peak-count time of 30 s and background-count time of 10 s. The instrument is also equipped with EDX system characterized by a detectable element range: Na to U, energy resolution: 144 eV and lithium (Li)-doped silicon single-crystal semiconductor detector. Several spot analyses (31) were collected to gain good analytical statistics because fibrous erionite bundles could be contaminated by other mineral phases and the chemical formula could be biased. Figure S1 in **Supplementary Material 1 reports** the points of the fiber bundles where the selected points were taken. Spot analyses were also conducted along the elongated fibers to verify chemical homogeneity. Out of the 31 collected points, 11 were selected for the calculation of the chemical formula. The statistics of these points is reported in Table S1 in **Supplementary Material 1**.

High-resolution transmission electron microscopy (HRTEM) imaging and three-dimensional electron diffraction (3DED) were performed with a JEOL JEM-F200 Multipurpose, working at 200 kV and equipped with a Schottky field emission gun (FEG) and a silicon drift detector (SDD) for EDX. HRTEM data were acquired by a Gatan RIO-16 CMOS camera (4k x4k pixel) and analyzed by Gatan Digital Micrograph software. EDX data were collected and quantified by

JEOL software. Electron diffraction data were recorded by an ASI Cheetah hybrid-pixel detector working in sequential mode at 24bit. 3DED data were collected in steps of 1°, with a nanobeam of about 30 nm obtained by inserting a 10 µm condenser aperture (Gemmi et al. 2019). Crystal tracking was performed in STEM mode. The beam was processed by a NanoMEGAS Topspin device, with a precession semi-angle of 1° (Mugnaioli et al. 2009). Exposure time for each diffraction pattern was 1 s. Camera length was 250 mm, equivalent in the direct space to a maximum resolution of about 0.7 Å. 3DED data were analyzed by the software PETS2 (Palatinus et al. 2019).

The specific surface area (SSA) of the sample was determined by N_2 adsorption/desorption isotherms using the ChemiSorb 2750 - Micromeritics instrument. Adsorption data were processed at the liquid nitrogen temperature (about –196 °C) following the standard Brunauer, Emmet and Teller (BET) method (Naderi 2015), and surface area was calculated as the average of three independent measurements on three different portions (approximately 500 mg) of sample. Before each measurement, the sample was conditioned at 50 °C under N_2 flow for about 30 min.

The ξ potential was determined both in distilled water and in organic Gamble's modified solution (Guldberg et al. 1998), the latter reproducing the intracellular alveolar lung fluid of the macrophage phago-lysosome environment. The measurements were conducted at pH=4.5 a 7.4 at 37 °C (the temperature of the body), using a ZetasizerNano Series instrument (Malvern). The pH of the suspensions was monitored using a Criston Series 2000 instrument.

For the structure refinement, X-ray powder diffraction (XRPD) data collected with a lab source and synchrotron radiation were merged. The same powder sample used for the two

experiments was obtained by cryogenic milling using a Retsch mixer mill MM 400 (Düsseldorf, Germany) equipped with two milling jars (35 mL) made of steel accompanied with a steel milling ball. The lining of the jar and balls is made of polytetrafluoroethylene (PTFE), which serves to prevent contamination of the sample with metals from the jar and balls during milling. Following the procedure described in Di Giuseppe et al. (2021a), the jars are filled with the sample in liquid nitrogen. When cooled, the jars are mounted in the mixer mill. During operation, jars oscillate from side to side with a pre-set frequency. For the experiment, the jars were loaded with 1 g of raw material and an oscillation frequency of 30 Hz was applied for 5 min. The lab experiment was conducted using a Bragg-Brentano PANalytical X'Pert Pro diffractometer, with a vertical circle Θ–Θ goniometer (240 mm radius), Cu Kα radiation, 40 kV and 40 mA and a Real Time Multiple Strip detector. Data were collected in reflection geometry with 1/2° fixed divergence and antiscatter slits and 0.02 rad soller slits. An integrated step scan of the detector of 0.013 °2Θ was used with a counting statistics of 180 s/step from 5 to 120 °2Θ. Synchrotron X-ray powder diffraction (XRPD) pattern for the structure refinement of the sample was collected at the Material Characterization by X-ray Diffraction Beamline (MCX), the synchrotron facility of ELETTRA (Trieste, Italy). The employed detector was a 4-circle Huber goniometer with a crystal analyzer/scintillation detector system, preceded by two slits with 200 and 300 μm vertical apertures. Measurements were performed at room temperature in transmission geometry using a borosilicate capillary (Ø=0.8 mm) and a fix wavelength of 0.8263 Å (i.e., 15 keV), in the 2–65° 2θ range, with data step of 0.008° 2θ and counting rate of 2.5 seconds per step. The Rietveld (Rietveld 1969) structure refinement using the two data sets was accomplished with the GSAS package (Larson and Von Dreele 2004) and its graphical interface

EXPGUI (Toby 2001). The starting structural model of erionite-K of Ballirano et al. (2009) was used and substantially modified during the refinement process. The background was modelled with a 12-terms Chebyschev function. The diffraction peak profiles were modelled using a pseudo-Voigt function with 1 Gaussian and 2 Lorentzian coefficients. The refinement included the unit-cell parameters, the phase fraction, the atomic coordinates, the atomic site occupancies for extra-framework positions or kept fixed to the value of atoms per formula unit determined by the EPMA data. Isotropic atomic displacement parameters were also refined in the later stages of the procedure. Soft constraints on tetrahedral bond lengths were imposed and used as additional observations with their weight progressively reduced to 5 in the later stages of the procedure. Difference Fourier maps were repeatedly calculated from the refined model and were useful for the location of residual electron density corresponding to extra-framework cations or H_2O molecules.

DETERMINATION OF THE TOXICITY/CARCINOGENICITY POTENTIAL OF THE SAMPLE USING THE FPTI MODEL

The Fiber Potential Toxicity Index (FPTI) model (Gualtieri 2018, 2021) was used to calculate the toxicity/carcinogenicity potential of the sample GD4a. The following parameters of the model are considered: morphometric parameters (mean fiber length and diameter, crystal habit and curvature, density, hydrophobic character, specific surface area), chemical parameters (iron content, content of ferrous iron, surface iron and its nuclearity, content of metals other than iron), biodurability related parameters (dissolution rate, rate of iron dissolution/release, rate of silica dissolution/release, rate of release of metals from the fiber), surface reactivity (zeta potential,

This is the peer-reviewed, final accepted version for American Mineralogist, published by the Mineralogical Society of America.
The published version is subject to change. Cite as Authors (Year) Title. American Mineralogist, in press.
DOI: https://doi.org/10.2138/am-2023-9184. http://www.minsocam.org/

aggregation state of the fibers in suspension, cation exchange capacity for fibrous zeolite species). For each parameter, a score is assigned depending on its measured value, susceptibility in inducing adverse effects, and weight (Gualtieri 2018). The $FPTI_i$ is calculated according to the equation (Gualtieri 2018):

$$FPTI_i = \sum_{i=1}^{n} w_1 \cdot w_2 \cdot T_i$$

with $w_1=1/H$ weight of the parameter according to its hierarchy H; $w_2=1/U$ weight of the parameter according to the uncertainty U of its determination; T_i=class value of the parameter i of the model. All the details of the model are explained in Gualtieri et al. (2021) and the WebFPTI manual available at fibers-fpti.unimore.it/FPTI/ which includes the calculation of the errors associated to each parameter.

RESULTS AND DISCUSSION

Chemical and morphological characterization

The TGA curve and its first derivative (DTG) show two distinct reactions (Fig. 3a), each of which occurs in two steps. The first reaction takes place between 25 and 350 °C with maximum reaction rates at 68 °C (step I, maximum on the DTG curve) and at about 165 °C (step II, shoulder on the DTG curve), with an overall mass change of 16.04 wt%. The second reaction, which is much less pronounced, is observed between 350 and 650 °C; the DTG curve shows a maximum (step I) at 435 °C and a shoulder (step II) at about 525 °C, with a total mass change of 2.71 wt%. No further changes are observed thereafter, and the overall mass changes at 800 °C is 19.06 wt%. The MSEGA curves show the release of H_2O (m/z=18) in the first reaction and H_2O

and CO_2 (m/z=44) in the second reaction (Fig. 3b). The water released in both reactions is attributable to the removal of water molecules within the zeolitic channel (Gottardi and Galli 1985; Ballirano et al. 2009; Ballirano and Cametti 2012; Bloise et al. 2016, 2017). This reaction develops over a rather wide thermal range (up to 450 °C: Ballirano et al. 2009) and the pattern of development, as well as the amount of total water released, depends essentially on the type and number of cations present in the zeolitic channels. The release of CO_2 is probably related to the presence of carbonaceous impurities as suggested by the higher temperature at which the reaction begins as better evidenced by the MSEGA curve (Fig. 3b). Because of the partial overlap of the water and carbon dioxide release, it is not possible to measure exactly the amount of zeolitic water released in this second reaction; however, considering the temperature of the start and end of gas release evidenced by the MSEGA curve, we can estimate a value of about 1.6 wt% of water. Consequently, the total amount of zeolitic water for sample GD4a can be estimated to be about 17.7 wt%, a value in good agreement with that determined in the above-mentioned studies (Gottardi and Galli 1985; Ballirano et al. 2009; Ballirano and Cametti 2012; Bloise et al. 2016, 2017)

The chemical formula calculated for sample GD4a using EMPA is:

$$(K_{2.63}Ca_{1.27}Mg_{0.98}Na_{0.37}Ba_{0.03}Sr_{0.01})[Si_{28.43}Al_{7.56}]_{35.99}O_{72}\cdot 29.07H_2O$$

Iron has been detected and measured with variable concentration but was intentionally excluded from both the framework and extraframework contents because it is assumed not to belong to the erionite structure as explained in Gualtieri et al. (2016) and discussed below.

The measured external surface area is 20.6(0.4) m^2/g. This value is higher than others documented in the literature data (8.14 m^2/g; Giordani et al. 2022; 10.1 m^2/g; Pacella et al. 2021)

345 likely because the fibers of the GD4A sample are smaller and the specific surface is higher than
346 that of the other erionite samples.

347 The morphology of sample GD4a was observed using SEM and TEM and consists of an
348 asbestiform crystal habit made up of long curly bundles (Fig. 4a) of nanometric erionite fibrils
349 (Fig. 4b). A morphometric analysis was conducted using approximately 100 measurements taken
350 from SEM and TEM images and is displayed in Table 1 and summarized in a series of
351 histograms as shown on Figure 5.

352 The fibers had a woolly appearance, with the length varying between 50 to 308 μm (average
353 210 μm). The results were similar for both fiber and fibril length. The width ranged between 2.7
354 to 30 μm (average 12 μm) for the bundles of fibers, however over 30% of the width fell between
355 5 - 7.5 μm. The fibrils typically had a much smaller width ranging between 0.34 μm to 3 μm
356 (average 1.36 μm). The mean size of the fibrils measured from the TEM data is even smaller
357 (0.39 μm), because what appears as a single fiber at SEM resolution often results as a bundle of
358 smaller fibers. As opposed to the morphometric data for the lengths and fiber width, the
359 distribution for fibril width was unimodal with ~50% of the fibrils between 1 to 1.5 μm. The
360 aspect ratio for fibers ranged between 4 to 99 (average 25) and the fibril aspect ratio ranged from
361 25 to 717 (average 171). These morphometric results indicate that while the fibers exceed the
362 maximum thickness requirements as outlined by WHO to be respirable, the fibrils are thin and
363 have the 3:1 aspect ratio to be considered a potential hazard (WHO 1986; 1997).

364 TEM morphometric measurements are in agreement with SEM data and show that the sample
365 is mostly composed of elongated fibers and bundles, generally shorter than 50 nm in thickness
366 and with lengths of several micrometers. The fibers are generally bent and tend to form bundles

(Fig. 6a). Fibers may undergo beam damage and can stand moderate HRTEM conditions only for few seconds. They become immediately amorphous when magnification gets above 150-200×. However, HRTEM images clearly show that fibers are crystalline (Fig. 6b). Some of them are single-crystals, with a certain bending through the fiber length. When single-crystal, the most recurrently visible interplanar distance is 11.0-11.6 Å, always parallel with the long side of the fiber. Sometimes it is possible to see a second interplanar distance perpendicular to the previous one, with value 15.0-15.3 Å, always parallel to the short fiber side. These distances correspond to the cell of erionite, with d_{100} = 11.2 Å and d_{001} = 15.1 Å. The main direction of fiber growth is then *c**, while it is reasonable to assume hexagonal cross-section of the fiber coherent with the *hk*0 plane. Rarely, some fibers show a periodicity of 7.5-7.6 Å. This may be coherent with offretite cell. However, this cell parameter appears always when the fiber has only 1D resolution, i.e. only the 00*l* line is visible in diffraction. In this condition, also erionite would show a periodicity of 7.5 Å, coherently with the presence of the 6_3 screw axis. It is therefore opinion of the authors that all HRTEM images can be explained with an erionite cell. Some fibers show disorder, with more domains growing one next to the other along the fiber length. Sometimes the occurrence of more domains results in fringed fiber terminations. It is worth to note that this disorder appears not immediately associable with supposed erionite/offretite alternation (as found for other samples in the literature: Gualtieri et al. 1998), which would be better imagined as an order-disorder sequence along *c**, i.e. along the fiber length. In between the fibers, flake-lake or lamellar particles are observed (Fig. 6c). This material is scarcely crystalline and only rarely it is possible to see some very disordered layer sequences with interspacing of about 10-12 Å.

389 Three 3DED data sets were collected from three different fibers which appeared well ordered
390 and larger than the average. After the reconstruction, all three data sets resulted consistent with
391 the erionite cell (Fig. 6d). No significant disorder was observed. The best date set delivered a
392 hexagonal cell with a = 13.2 Å and c = 15.1 Å. Extinctions consistent with space group $P6_3/mmc$
393 can be recognized in the reconstructed 2D diffraction patterns. The best data set was also used
394 for a tentative *ab initio* structure determination by direct methods implemented in SIR2014
395 (Burla et al. 2014). The framework of erionite was immediately detected, together with the clear
396 localization of K and possibly partially occupied Ca/Na ions and water molecules in the cavities.
397 Energy dispersive spectroscopy (EDS) spot analyses confirmed that the fibers are mostly
398 made of Si and O. Al is invariably present generally together with K and Ca. Na, Mg, and Cl
399 peaks are also generally detected but are very weak (see **Supplementary Material 2**). EDS
400 analyses were not performed with an analytical holder, and therefore the peak of Fe is always
401 present, together with Cr and Co. With the present data, we suggest to consider Fe as an artefact
402 when present with less than 2%wt. No EDS points from the fibers show an Fe signal higher than
403 2%. On the other hand, EDS analyses from flake-like material show a considerably increase in
404 Fe, Al, Mg and sometimes Ca (see **Supplementary Material 2**).
405 To summarize, the TEM study indicates that all inspected fibers are probably erionite, and
406 specifically erionite-K (possibly also erionite-Ca in some cases). They show a high degree of
407 crystallinity and fibrous-asbestiform habit. The source of iron in the sample is not from iron-
408 oxides or hydroxides particles but from flakes of layer silicates, possibly a smectite-rich phase
409 like nontronite, as already observed for other natural asbestiform erionites (Gualtieri et al. 2016).

XRPD data confirmed that the specimen contains about 2 wt% of smectite and illite. Other impurities are below the detection limit of X-ray diffraction. Figure 7 reports the fit obtained by the Rietveld refinement of the GD4a erionite sample while Table S3 of the **Supplementary Material 3** reports the refinement statistics, calculated unit cell and structural parameters. Pointing out that the site population of the sites occupied by Mg, Na, Ba and Al were fixed to the values of the formula calculated from the EPMA data and that Sr was not considered, the chemical composition from the final refinement was

$$(K_{2.57}Ca_{1.35}Mg_{0.98}Na_{0.37}Ba_{0.03})[Si_{28.44}Al_{7.56}]_{36}O_{72}\cdot 29.48H_2O$$

The formula should be compared to that calculated from the EPMA data:

$$(K_{2.63}Ca_{1.27}Mg_{0.98}Na_{0.37}Ba_{0.03}Sr_{0.01})[Si_{28.43}Al_{7.56}]_{35.99}O_{72}\cdot 29.07H_2O$$

Due to the great disorder of the water molecules, only the oxygen atoms were located and the hydrogens atoms of the water molecules were not positioned. The relevant bond distances are shown in Table 2. The full set of bond distances and angles are available upon request to the authors.

The two independent tetrahedral sites *T*1 and *T*2 are occupied by Si and Al in a disordered way and build the D6R and S6R cages, respectively. The mean bond distances $\langle T1 — O\rangle$ = 1.6376Å and $\langle T2—O\rangle$ = 1.646575Å indicate a negligible difference between the mean [T—O] distances of the two tetrahedral sites, with a very small preference of Al for *T*2 compared with *T*1 (0.14). Individual *T*—O—*T* angles, not reported here but available upon request to the authors, show no significant deviation from the values described by Gualtieri et al. (1998), Ballirano et al. (2009), and Giacobbe et al. (2023).

Regarding the extraframework cations, their disordered distribution and the presence of nearly isoelectronic species required the use of prior information on the chemical composition and the expected coordination of the cations to locate them. The species were hence assigned based on the coordination and the distances from the surrounding oxygen atoms of the framework and water molecules of the candidate cations, taking advantage of the EPMA chemical data. The cancrinite cage hosts the K1 atomic position with nearly a full site occupancy (Table S3) and a 12-fold coordination with 6 oxygen O2 atoms and 6 oxygen O3 atoms (Table 2). This site in the special position 0 0 ¼ is a key templating agent of the erionite framework because it is invariably present and almost fully occupied by K^+ in the cancrinite cage of all the natural erionite structure models from the literature regardless of their composition (erionite-Ca, erionite-Na or erionite-K). With the exception of Ballirano et al. (2009) for erionite-K from Oregon, all the natural erionite structure models report a 12–fold coordination with a group of 6 shorter distances from the framework oxygen O2 atoms and 6 longer distances from the oxygen O3 atoms (Alberti et al. 1997; Gualtieri et al. 1998, 2016; Cametti et al. 2013; Quiroz-Estrada et al. 2020; Battiston et al. 2022; Giacobbe et al. 2023; Mattioli et al. 2023). When the value of the K1–O2 distances are close to the value of the K1–O3 distances, like in our erionite structure, the coordination sphere is more symmetrical, resembling a spherical shape (see the case (a) in Fig. 8). On the other hand, when the value of the K1–O2 distances departs from to the value of the K1–O3 distances, as observed for other erionite structure models, the coordination gets closer to a hexagonal prism with two layers of oxygen atoms at more or less the same height (see the case (b) in Fig. 8). Other K^+ atoms were located in the big erionite cavity in correspondence with the K2 and K3 special positions at 0.5 0 0 and 1/3 2/3 0.1135, respectively. Again, K^+ atoms display a 12–fold

453 coordination with both framework oxygen atoms and H_2O molecules (see Table 2 considering
454 that 2 out of 4 OW3 sites are mutually exclusive). It is the first time that residual K^+ is refined in
455 a position different from K2. In fact, literature data invariably reports residual K^+, if found, in the
456 K2 site in the erionite cavity (Ballirano et al. 2009; Battiston et al. 2022; Giacobbe et al. 2023;
457 Mattioli et al. 2023) with a distorted 12–fold coordination of framework oxygen atoms and H_2O
458 molecules. The refined position K3 corresponds to the Ca2 site in Alberti et al. (1997), Ballirano
459 et al. (2009), Cametti et al. (2013), Gualtieri et al. (2016), Quiroz-Estrada et al. (2020), Battiston
460 et al. (2022), and Mattioli et al. (2023). K3 instead corresponds to the Ca1 site in Gualtieri et al.
461 (1998) and Giacobbe et al. (2023).

462 In our erionite structure model, extraframework cations other than K^+ (Ca^{2+} with minor Na^+
463 and Ba^{2+}) were located inside the big erionite cavity in the Ca1 and Ca2 special positions (Table
464 S3). The refined position Ca1 corresponds to the Ca1 site in Alberti et al. (1997), Ballirano et al.
465 (2009), Cametti et al. (2013), Gualtieri et al. (2016), Quiroz-Estrada et al. (2020), Battiston et al.
466 (2022), and Mattioli et al. (2023). Ca1 instead corresponds to the Ca2 site in Gualtieri et al.
467 (1998) and Giacobbe et al. (2023). A 6– to 9–fold coordination with H_2O molecules (see Table 2
468 considering that 3 out of 6 OW3 sites are mutually exclusive) is calculated for the Ca1 position.
469 When Na^+ occupies that site, the coordination number is 6. The refined position Ca2 corresponds
470 to the Ca3 site in Alberti et al. (1997), Ballirano et al. (2009), Cametti et al. (2013), Gualtieri et
471 al. (2016), Quiroz-Estrada et al. (2020), Battiston et al. (2022), and Mattioli et al. (2023). A 9–
472 fold coordination with H_2O molecules (see Table 2 again considering that 3 out of 6 OW3 sites
473 are mutually exclusive) is calculated for the Ca2 position when both Ca^{2+} and Ba^{2+} occupy that
474 position.

475 Extraframework magnesium atoms deserve a dedicated discussion. Figure 9a is a standard
476 compositional plot used to classify erionite (black triangles) and offretite (black circles) samples
477 from the extraframework cation content. Data points are taken from the literature (Alberti et al.
478 1997; Gualtieri et al. 1998, 2016; Ballirano et al. 2009; Cametti et al. 2013; Quiroz-Estrada et al.
479 2020; Battiston et al. 2022; Giacobbe et al. 2023; Mattioli et al. 2023) and show that the
480 asbestiform erionite from Gawler Downs (black cross) is anomalous, with a quite unique content
481 of K^+ and Mg^{2+}. Figure 9b is a plot derived from the data plotted in Figure 9a showing the
482 calculated ratio Mg/(Ca+Na+K) for each sample. This parameter permits a better discrimination
483 between the erionite and the offretite families. Erionites (white bars) display a mean
484 Mg/(Ca+Na+K)=0.06 with a maximum value of 0.2282. Offretites (black bars) display a mean
485 Mg/(Ca+Na+K)=0.475 with a minimum value of 0.2808. The GD4a sample from New Zealand
486 (gray bar) displays a Mg/(Ca+Na+K)=0.2248 and its inclusion in the family of erionite is fully
487 justified. Despite the high content of magnesium in the GD4a sample, there is no evidence of
488 offretite nor erionite-offretite disordered sequences as observed for other Mg-rich samples like
489 the erionite from Araules (Ht. Loire, France) with Mg=0.83 a.f.u. (Gualtieri et al. 1998). Mg^{2+} is
490 located in the erionite cavity surrounded by a cloud of H_2O molecules. The best configuration is
491 in a 6–fold coordination with 3 out of the 6 mutually exclusive H_2O molecules OW3 at 2.092 Å
492 and 3 H_2O molecules OW7 at 1.897 Å (Fig. 10 and Table 2). Alternatively, another
493 configuration with 3 H_2O molecules OW3 at 2.092 Å and 3 H_2O molecules OW5 at 2.423 Å is
494 also possible but much more distorted. In agreement, a survey of the existing structure models of
495 erionite from the literature shows that Mg^{2+} is mostly found inside the erionite cavity, at different
496 height along the principal crystallographic axis, and surrounded by 6 H_2O molecules. It is in the

position corresponding to Ca2 site with 3 H_2O molecules at 1.91 Å and 3 H_2O molecules at 2.28 Å in erionite-Ca from Shourdo (Georgia) (Gualtieri et al. 1998); in the Ca2 site with 3 H_2O molecules at 2.19 Å and 3 H_2O molecules at 2.76 Å in erionite-Ca from Agate beach (Oregon, USA) (Gualtieri et al. 1998); in the Ca1 site with 3 H_2O molecules at 1.88 Å and 3 H_2O molecules at 2.68 Å in erionite-Na from Durkee (Oregon, USA) (Cametti et al. 2013); in the Ca3 site with 3 H_2O molecules at 2.20 Å and 3 H_2O molecules at 2.25 Å in erionite-K from Tuzköy (Turkey; Giacobbe et al. 2023). Crystallographic sites hosting Mg^{2+} atoms refined inside the erionite cavity but surrounded by a disordered solvation sphere of water molecules were also calculated: Ballirano et al. (2009) found evidence of Mg^{2+} in the Ca1 site with 2 H_2O molecules at 2.05 Å, 2.16 Å, 2.17 Å, and 2.37 Å, respectively, in erionite-K from Rome (Oregon, USA); Quiroz-Estrada et al. (2020) refined Mg^{2+} in the Ca1 site with 3 H_2O molecules at 1.79 Å and 2.40 Å, respectively, and 6 H_2O molecules at 1.97 Å and 2.44 Å, respectively, in erionite-Na from Agua Prieta (Sonora, Mexico); Battiston et al. (2022) refined Mg^{2+} in the Ca1 site with 3 H_2O molecules at 1.86 Å and 6 H_2O molecules at 2.51 Å, respectively, in erionite-K from Chase Creek, Falkland, British Columbia (Canada); finally Mattioli et al. (2023) refined Mg^{2+} in the Ca1 site with 3 H_2O molecules at 2.22 Å, 2.29 Å, and 2.49 Å, respectively, in erionite-K from Poggio Nibbio (Latium, Italy). A sample from the same locality but classified as erionite-Na displayed Mg^{2+} in the Ca1 site with 3 H_2O molecules at 2.22 Å, 2.32 Å, 2.42 Å, and 2.44 Å, respectively. The analysis of the coordination sphere of Mg^{2+} does not correlate with the Mg-content nor the chemical nature of the erionite sample.

Sample GD4a was also analysed using micro-Raman with the spectrum reported in Figure 11 (middle curve). The spectrum is compared to that of a pure erionite-K from Rome, Oregon

519 (USA; top curve) and a pure offretite from Saviore (Brescia, Italy; bottom curve) in the Raman
520 shift region 100 to 1400 cm^{-1} (Giacobbe et al. 2023). GD4a shows bands at 170, 270, 355 (?),
521 468, 482, 569, 595, 699, and 1100 cm^{-1} in the investigated region. The erionite-K sample from
522 Oregon shows bands at 355, 470, 486, and 595 cm^{-1} while the offretite sample shows bands at
523 140, 270 (?), 429, 467, 495, and 559 cm^{-1}. Based on the existing literature on the Raman
524 spectroscopy of natural zeolites, it is possible to interpret the observed bands in terms of
525 molecular vibrational modes. The weak band at 170 cm^{-1} is tentatively assigned to the bending
526 vibrational mode δ of the O—T—O bonds (Brémard and Le Maire 1993); the very weak bands
527 at 270 and 355 cm^{-1} are assigned to the symmetric bending vibrational modes δ_S of the T—O—T
528 bonds in the double 6-membered (*d6r*) rings and to the antisymmetric bending vibrational modes
529 δ_a of the T—O—T bonds in the double 6-membered (*d6r*) rings, respectively (Wang et al. 2019);
530 the intense bands at 467 and 486 cm^{-1} are assigned to the symmetric bending vibrational modes
531 δ_S of the T—O—T bonds in the 6-membered rings and to the symmetric bending vibrational
532 modes δ_S of the T—O—T bonds in the 4-membered rings, respectively (Mozgawa 2001; Croce
533 et al. 2013); the bands at 569 and 595 cm^{-1} are tentatively assigned to the antisymmetric bending
534 vibrational modes δ_a of the T—O—T bonds in the 6-membered rings and to the antisymmetric
535 bending vibrational modes δ_a of the T—O—T bonds in the 4-membered rings, respectively; the
536 band at 698 cm^{-1} is assigned to the symmetric stretching mode υ_s of the T—O bonds (Lercher and
537 Jentys 2007); the weak band at 1100 cm^{-1} is assigned to the antisymmetric stretching mode υ_a of
538 the T—O bonds (Giacobbe et al. 2023). The spectrum of the GD4a sample, with the major bands
539 at 468, 482 and 569 cm^{-1} is much closer to that of erionite-K from Oregon and the signals
540 reported for the Tuzköy (Turkey) and Jersey (USA) fibrous erionites published by Giacobbe et

al. (2023), showing the major bands at 468, 488-489, and 569-571 cm^{-1}. Rinaudo and Croce (2019) also reported that the major distinctive bands of erionite-K from Oregon are at 471, 486, and 569 cm^{-1} supporting the interpretation that the GD4a sample is actually erionite. In fact, the GD4a sample does not show the major bands of offretite at 429 and 467 cm^{-1} (Fig. 11 bottom) observed at 431 and 465 cm^{-1} by Giacobbe et al. (2023).

Overall, the analytical techniques have determined that sample GD4a is erionite-K, with a unique composition. This is supported by the micro-Raman data spectrum which shows very similar bands to the erionite-K standard from Oregon (Giacobbe et al. 2023). Furthermore the sample has an asbestiform crystal habit as seen within the SEM images and the fibrils are in agreement with the WHO (1986, 1997) requirements for respirable fibers . TGA estimated the zeolitic water to be 17.7 wt%, a value typically seen within zeolites. The EPMA calculation for the GD4a chemical formula is also in agreement with other occurrences of erionite however this sample has a slightly higher Mg^{2+} content. TEM suggested the presence of layer silicates on the surface of erionite fibers and this is confirmed by XRPD data which denotes the presence of smectite and illite.

MODEL OF POTENTIAL TOXICITY/CARCINOGENICITY

To assess the potential toxicity/carcinogenicity of the asbestiform erionite GD4a sample, we used the FPTI model (Gualtieri 2018, 2021) which has been applied to a suite of mineral fibers (*e.g.* fibrous glaucophane: Di Giuseppe et al. 2019, Russian chrysotile: 2021a) in the attempt to predict their ability to induce adverse effects *in vitro*/*in vivo* (Mossman and Gualtieri 2020). For the calculation, the model considers all the physical-crystal-chemical parameters responsible for

563 adverse effects including morphometric parameters, chemical parameters, biodurability-related
564 parameters, and surface reactivity.

565 In terms of morphometric parameters, a key factor of carcinogenicity is the length and width
566 of the erionite fibres (Gualtieri 2018, 2021). Images from SEM and TEM have displayed that
567 sample GD4a is made up of thick fibres (mean ~12.07 μm) split into nanometric fibrils with a
568 mean width of 1.36 μm (SEM) and 0.39 μm (TEM), the length is 206 μm. The fibres are not
569 respirable, however if the sample splits into much smaller respirable fibrils, they could
570 potentially be carcinogenic due to their ≤ 3 μm diameter and ≥ 3:1 length to width ratio (mean
571 ratio is 171 μm; see Table 1). The splitting of the fibres has also resulted in a higher surface area
572 to volume ratio which can increase the surface reactivity of the sample (Dogan et al. 2008;
573 Gualtieri 2023). Regarding chemical parameters, the sample from Gawler Downs contain no iron
574 within its chemical structure, iron exists only in the form of layer silicates on the surface of the
575 fibers, negating some of the toxic effects that may occur (Gualtieri 2018). More detailed
576 information on the dataset used for the FPTI calculation can be found in **Supplementary**
577 **Material 4**, which shows the exact values used for the calculation.

578 The FPTI value calculated for the GD4a sample is 2.28(4). This value must be compared to
579 those available for other asbestiform fibrous-erionites from Karain (Turkey: Lowers et al. 2010)
580 and Jersey (Nevada, USA: Gualtieri et al. 2016), a positive carcinogenic standard UICC
581 crocidolite (Gualtieri 2012) and the negative (non-carcinogenic) standard NYAD G (1)
582 wollastonite (Fig. 12: Di Giuseppe et al. 2021b). The calculated value is comparable to that of
583 the other erionites (2.33(7) and 2.28(21) for Karain and Jersey samples, respectively),
584 significantly lower than the value of the positive standard UICC crocidolite (2.73(8)) and well

585 above the value of the negative wollastonite standard (1.9(1)). The minor difference with respect
586 to the carcinogenic Karain fiber from Turkey is likely due to a lower content of toxic metals that
587 can be exchanged *in vitro/vivo*.
588
589 **IMPLICATIONS**
590 An important implication from this study is that erionite from Gawler Downs is a health
591 hazard comparable to other asbestiform erionites that have been investigated in other parts of the
592 world. This is evident by the analytical data which displays key morphometric features
593 compatible with carcinogenic erionite. One such key feature is the size and length of the erionite
594 fibers. The mean width of GD4a fibers was 12.07 μm, however the mean fibril width was 1.36
595 μm under SEM and 0.39 μm under TEM, both of which are ≤ 3 μm. The mean length of the
596 fibrils was 206.82 μm and the L_r/W_r was 171.05 (an aspect ratio ≥ 3:1). These dimensions
597 indicate that the erionite fibrils, if separated from the fibers, are potentially respirable according
598 to the WHO criteria (IARC 2002; Mossman et al. 2011). Furthermore, the FPTI calculation also
599 indicates that GD4a has a similar toxicity potential to other carcinogenic erionites, for example
600 erionite from Karain, Turkey (Dogan and Dogan 2008) whose composition which resulted in
601 cases of malignant mesothelioma was erionite-K and erionite-Na (Dogan and Dogan 2008;
602 Dogan et al. 2008). Although further studies need to take place, there is the possibility that
603 different types of erionite may cause a variance in toxicity. The composition of sample GD4a is
604 most closely aligned to that of erionite-K, indicating potassium is the most abundant extra
605 framework cation within the chemical structure and the formula calculated with EPMA is
606 $K_{2.63}Ca_{1.27}Mg_{0.98}Na_{0.37}Ba_{0.03}Sr_{0.01}[Si_{28.43}Al_{7.56}]_{35.99}O_{72}\cdot 29.07H_2O$. The erionite contained a high

607 degree of Mg^{2+}, more than what erionite typically contains. Nevertheless, further comparisons
608 with other known erionite and offretite samples have indicated that GD4a is indeed erionite, with
609 a unique content of K^{+} and Mg^{2+} and contains no offretite or disordered erionite-offretite
610 sequences within the mineral.

611 Erionite is only a hazard when it becomes airborne due to disturbances such as erosive
612 processes or human activities making it airborne. The erionite fibers were found to be localized
613 to open vesicles in the andesite-dacite formation. The Gawler Downs area has a low population
614 density and is mostly farmland, with potential sources of disturbance to the erionite fibers being
615 quad-biking, or vegetation clearance and disturbance from foot or animal traffic, as these
616 activities have been proven to cause the aerosolization of mineral fibers (Beaucham et al. 2018).
617 Aeolian processes and frost heave are known to occur in the region of Gawler Downs due to its
618 climate, and these processes have the ability to liberate mineral fibers within the landscape into
619 the air (McGowan et al. 1996).

620 The results from this study have indicated that asbestiform erionite-K at Gawler Downs is
621 composed of fibers and fibrils, some of which are within the hazardous range for mineral fibers.
622 In order to quantify the health implications for this location, further work is required to
623 determine the effect that erosional processes have on the mineral, and any liberation into the air.
624

625 **ACKNOWLEDGMENTS**

626 This work was funded by MBIE project 3721404: assessing and managing the risk of
627 carcinogenic erionite in New Zealand. The work was also supported through a Royal Society of
628 New Zealand Catalyst Seed grant 20-UOA-016-CSG (to MB) and through the University of

Auckland Doctoral scholarship scheme (to JP). This work was also supported by the PRIN project fund "*Fibres: a multidisciplinary mineralogical, crystal-chemical and biological project to amend the paradigm of toxicity and cancerogenicity of mineral fibres*" (PRIN: Progetti di Ricerca di Rilevante Interesse Nazionale—Bando 2017—Prot. 20173X8WA4). Andrea Risplendente (University of Milan) is kindly acknowledged for help during the EPMA analytical session. We warmly thank the four anonymous referees of this work for their careful and constructive revision.

REFERENCES CITED

Alberti, A., Martucci, A., Galli, E., and Vezzalini, G. (1997) A reexamination of the crystal structure of erionite. Zeolites, 19, 349–352.

Armbruster, T., and Gunter, M.E. (2001) Crystal Structures of Natural Zeolites. Reviews in Mineralogy and Geochemistry, 45, 1–67.

Baerlocher, C., McCusker, L.B., and Olson, D.H. (2007) ERI - P63/mmc. In C. Baerlocher, L.B. McCusker, and D.H. Olson, Eds., Atlas of Zeolite Framework Types (Sixth Edition) pp. 128–129. Elsevier Science B.V., Amsterdam.

Ballirano, P., and Cametti, G. (2012) Dehydration dynamics and thermal stability of erionite-K: Experimental evidence of the "internal ionic exchange" mechanism. Microporous and Mesoporous Materials, 163, 160–168.

Ballirano, P., Andreozzi, G.B., Dogan, M., and Dogan, A.U. (2009) Crystal structure and iron topochemistry of erionite-K from Rome, Oregon, U.S.A. American Mineralogist, 94, 1262–1270.

Ballirano, P., Bloise, A., Gualtieri, A.F., Lezzerini, M., Pacella, A., Perchiazzi, N., Dogan, M., and Dogan, A.U. (2017) The crystal structure of mineral fibres. In A.F. Gualtieri, Ed.,

653 Mineral fibres: Crystal chemistry, chemical-physical properties, biological interaction and
654 toxicity pp. 17–64. Mineralogical Society of Great Britain & Ireland.

655 Bariş, B., Demir, A.U., Shehu, V., Karakoca, Y., Kisacik, G., and Bariş, Y.I. (1996)
656 Environmental fibrous zeolite (erionite) exposure and malignant tumors other than
657 mesothelioma. Journal of Environmental Pathology, Toxicology and Oncology: Official Organ
658 of the International Society for Environmental Toxicology and Cancer, 15, 183–189.

659 Battiston, T., Comboni, D., Pagliaro, F., Lotti, P., Hanfland, M., and Gatta, G.D. (2022) High-
660 pressure behavior and crystal-fluid interaction in natural erionite-K. Materials Chemistry and
661 Physics, 292, 126760.

662 Beaucham, C., King, B., Feldmann, K., Harper, M., and Dozier, A. (2018) Assessing
663 occupational erionite and respirable crystalline silica exposure among outdoor workers in
664 Wyoming, South Dakota, and Montana. Journal of Occupational and Environmental Hygiene,
665 15, 455–465.

666 Bloise, A., Catalano, M., Barrese, E., Gualtieri, A.F., Bursi Gandolfi, N., Capella, S., and
667 Belluso, E. (2016) TG/DSC study of the thermal behaviour of hazardous mineral fibres. Journal
668 of Thermal Analysis and Calorimetry, 123, 2225–2239.

669 Bloise, A., Kusiorowski, R., Gualtieri, M.L., and Gualtieri, A.F. (2017) Thermal behaviour of
670 mineral fibres. In A. F. Gualtieri, Ed., Mineral Fibres: Crystal Chemistry, Chemical-Physical
671 Properties, Biological Interaction and Toxicity Vol. 18, pp. 215–260. Mineralogical Society of
672 Great Britain & Ireland.

673 Brémard, C., and Le Maire, M. (1993) Low-frequency Raman spectra of dehydrated faujasitic
674 zeolites. The Journal of Physical Chemistry, 97, 9695–9702.

675 Brook, M.S., Black, P.M., Salmond, J., Dirks, K.N., Berry, T.-A., and Steinhorn, G. (2020)
676 Erionite in Auckland bedrock and malignant mesothelioma: an emerging public and occupational
677 health hazard? The New Zealand Medical Journal, 133, 73–78.

678 Cametti, G., Pacella, A., Mura, F., Rossi, M., and Ballirano, P. (2013) New morphological,
679 chemical, and structural data of woolly erionite-Na from Durkee, Oregon, U.S.A. American
680 Mineralogist, 98, 2155–2163.

681 Croce, A., Musa, M., Allegrina, M., Rinaudo, C., Baris, Y.I., Dogan, A.U., Powers, A.,
682 Rivera, Z., Bertino, P., Yang, H., and others (2013) Micro-Raman spectroscopy identifies
683 crocidolite and erionite fibers in tissue sections. Journal of Raman Spectroscopy, 44, 1440–1445.

684 Di Giuseppe, D., Harper, M., Bailey, M., Erskine, B., Della Ventura, G., Ardit, M., Pasquali,
685 L., Tomaino, G., Ray, R., Mason, H., and others (2019) Characterization and assessment of the
686 potential toxicity/pathogenicity of fibrous glaucophane. Environmental Research, 178, 108723.

687 Di Giuseppe, D., Zoboli, A., Nodari, L., Pasquali, L., Sala, O., Ballirano, P., Malferrari, D.,
688 Raneri, S., Hanuskova, M., and Gualtieri, A.F. (2021a) Characterization and assessment of the
689 potential toxicity/pathogenicity of Russian commercial chrysotile. American Mineralogist, 106,
690 1606–1621.

691 Di Giuseppe, D., Scognamiglio, V., Malferrari, D., Nodari, L., Pasquali, L., Lassinantti
692 Gualtieri, M., Scarfì, S., Mirata, S., Tessari, U., Hanuskova, M., and others (2021b)
693 Characterization of Fibrous Wollastonite NYAD G in View of Its Use as Negative Standard for
694 In Vitro Toxicity Tests. Minerals, 11, 1378.

695 Dogan, A.U., and Dogan, M. (2008) Re-evaluation and re-classification of erionite series
696 minerals. Environmental Geochemistry and Health, 30, 355–366.

697 Dogan, A.U., Dogan, M., and Hoskins, J.A. (2008) Erionite series minerals: mineralogical
698 and carcinogenic properties. Environmental Geochemistry & Health, 30, 367–381.

699 Field, B.D., and Browne, G.H. (1989) Cretaceous and Cenozoic Sedimentary Basins and
700 Geological Evolution of the Canterbury Region, South Island, New Zealand, 94 p. New Zealand
701 Geological Survey.

Giacobbe, C., Moliterni, A., Di Giuseppe, D., Malferrari, D., Wright, J.P., Mattioli, M., Raneri, S., Giannini, C., Fornasini, L., Mugnaioli, E., and others (2023) The crystal structure of the killer fibre erionite from Tuzköy (Cappadocia, Turkey). IUCrJ, 10, 397–410.

Giordani, M., Mattioli, M., Dogan, M., and Dogan, A.U. (2016) Potential carcinogenic erionite from Lessini Mounts, NE Italy: Morphological, mineralogical and chemical characterization. Journal of Toxicology and Environmental Health, Part A, 79, 808–824.

Giordani, M., Mattioli, M., Ballirano, P., Pacella, A., Cenni, M., Boscardin, M., and Valentini, L. (2017) Geological occurrence, mineralogical characterization, and risk assessment of potentially carcinogenic erionite in Italy. Journal of Toxicology and Environmental Health, Part B, 20, 81–103.

Giordani, M., Mattioli, M., Cangiotti, M., Fattori, A., Ottaviani, M.F., Betti, M., Ballirano, P., Pacella, A., Di Giuseppe, D., Scognamiglio, V., and others (2022) Characterisation of potentially toxic natural fibrous zeolites by means of electron paramagnetic resonance spectroscopy and morphological-mineralogical studies. Chemosphere, 291, 133067.

Gottardi, G., and Galli, E. (1985) Zeolites with 6-rings. In G. Gottardi and E. Galli, Eds., pp. 168–222. Springer-Verlag, Berlin, Heidelberg.

Gualtieri, A., Artioli, G., Passaglia, E., Bigi, S., Viani, A., and Hanson, J.C. (1998) Crystal structure-crystal chemistry relationships in the zeolites erionite and offretite. American Mineralogist, 83, 590–606.

Gualtieri, A.F. (2012) 7 - Mineral fibre-based building materials and their health hazards. In F. Pacheco-Torgal, S. Jalali, and A. Fucic, Eds., Toxicity of Building Materials pp. 166–195. Woodhead Publishing.

Gualtieri, A.F. (2018) Towards a quantitative model to predict the toxicity/pathogenicity potential of mineral fibers. Toxicology and Applied Pharmacology, 361, 89–98.

726 ——— (2021) Bridging the gap between toxicity and carcinogenicity of mineral fibres by
727 connecting the fibre crystal-chemical and physical parameters to the key characteristics of
728 cancer. Current Research in Toxicology, 2, 42–52.

729 ——— (2023) Journey to the centre of the lung. The perspective of a mineralogist on the
730 carcinogenic effects of mineral fibres in the lungs. Journal of Hazardous Materials, 442, 130077.

731 Gualtieri, A.F., Gandolfi, N.B., Pollastri, S., Pollok, K., and Langenhorst, F. (2016) Where is
732 iron in erionite? A multidisciplinary study on fibrous erionite-Na from Jersey (Nevada, USA).
733 Scientific Reports, 6, 37981.

734 Gualtieri, A.F., Leoncini, M., Rinaldi, L., Zoboli, A., and Di Giuseppe, D. (2021) WebFPTI:
735 A tool to predict the toxicity/pathogenicity of mineral fibres including asbestos. Earth Science
736 Informatics, 14, 2401–2409.

737 Guldberg, M., Christensen, V.R., Perander, M., Zoitos, B., Koenig, A.R., and Sebastian, K.
738 (1998) Measurement of in- vitro fibre dissolution rate at acidic pH. The Annals of Occupational
739 Hygiene, 42, 233–243.

740 Harada, K., Iwamoto, S., and Kihara, K. (1967) Erionite, Phillipsite and Gonnardite in the
741 Amygdales of Altered Basalt from Maze, Niigata Prefecture, Japan. American Mineralogist, 52,
742 1785–1794.

743 IARC (1997) Erionite, IARC Monographs on the evaluation of the carcinogenic risk of
744 chemicals to humans pp. 225–239.

745 ——— (2002) Man-made Vitreous Fibres. International Agency for Research on Cancer.

746 Larson, A.C., and Von Dreele, R.B. (2004) General Structure Analysis System (GSAS). 86-
747 748, Los Alamos National Laboratory, New Mexico.

748 Lercher, J., and Jentys, A. (2007) Infrared and raman spectroscopy for characterizing zeolites.
749 Studies in Surface Science and Catalysis, 168, 435–476.

Lowers, H., Adams, D.T., Meeker, G.P., and Nutt, C.J. (2010) Chemical and morphological comparison of erionite from Oregon, North Dakota, and Turkey. USGS Numbered Series, U.S. Geological Survey.

Mattioli, M., Giordani, M., Ballirano, P., Salvioli-Mariani, E., Bernardini, S., and Ventura, G.D. (2023) First occurrence, crystal-chemistry and structure of erionite, a carcinogenic fibrous zeolite, from the volcanic rocks of Latium (Italy). Periodico di Mineralogia, 92, 159–178.

McCusker, L.B., Liebau, F., and Engelhardt, G. (2001) Nomenclature of structural and compositional characteristics of ordered microporous and mesoporous materials with inorganic hosts(IUPAC Recommendations 2001). Pure and Applied Chemistry, 73, 381–394.

McGowan, H.A., Sturman, A.P., and Owens, I.F. (1996) Aeolian dust transport and deposition by foehn winds in an alpine environment, Lake Tekapo, New Zealand. Geomorphology, 15, 135–146.

Mossman, B.T., and Gualtieri, A.F. (2020) Lung Cancer: Mechanisms of Carcinogenesis by Asbestos. In S. Anttila and P. Boffetta, Eds., Occupational Cancers pp. 239–256. Springer International Publishing, Cham.

Mossman, B.T., Lippmann, M., Hesterberg, T.W., Kelsey, K.T., Barchowsky, A., and Bonner, J.C. (2011) Pulmonary endpoints (lung carcinomas and asbestosis) following inhalation exposure to asbestos. Journal of Toxicology and Environmental Health. Part B, Critical Reviews, 14, 76–121.

Mozgawa, W. (2001) The relation between structure and vibrational spectra of natural zeolites. Journal of Molecular Structure, 596, 129–137.

Naderi, M. (2015) Chapter Fourteen - Surface Area: Brunauer–Emmett–Teller (BET). In S. Tarleton, Ed., Progress in Filtration and Separation pp. 585–608. Academic Press, Oxford.

Oliver, P.J. (1977) The Mesozoic geology of the Mt Somers area, Canterbury: including geochemical and paleomagnetic studies of the Cretaceous calc-alkaline Mt Somers volcanics. Ph.D thesis, University of Canterbury, Christchurch, New Zealand.

Oliver, P.J., and Keene, H.W. (1989) Sheet K36 AC and part Sheet K35. Department of Scientific and Industrial Research, Wellington.

Pacella, A., Ballirano, P., Fantauzzi, M., Rossi, A., Viti, C., Arrizza, L., Nardi, E., Caprioli, R., and Montereali, M.R. (2021) Surface and Bulk Modifications of Fibrous Erionite in Mimicked Gamble's Solution at Acidic pH. Minerals, 11, 914.

Passaglia, E., and Sheppard, R.A. (2001) The Crystal Chemistry of Zeolites. Reviews in Mineralogy and Geochemistry, 45, 69–116.

Passaglia, E., Artioli, G., and Gualtieri, A. (1998) Crystal chemistry of the zeolites erionite and offretite. American Mineralogist, 83, 577–589.

Patel, J.P., and Brook, M.S. (2021) Erionite asbestiform fibres and health risk in Aotearoa/New Zealand: A research note. New Zealand Geographer, nzg.12291.

Patel, J.P., Brook, M.S., Kah, M., and Hamilton, A. (2022) Global geological occurrence and character of the carcinogenic zeolite mineral, erionite: A review. Frontiers in Chemistry, 10.

Quiroz-Estrada, K., Pacella, A., Ballirano, P., Hernández-Espinosa, M.Á., Felipe, C., and Esparza-Schulz, M. (2020) Crystal Chemical and Structural Characterization of Natural and Cation-Exchanged Mexican Erionite. Minerals, 10, 772.

Rietveld, H.M. (1969) A profile refinement method for nuclear and magnetic structures. Journal of Applied Crystallography, 2, 65–71.

Rinaudo, C., and Croce, A. (2019) Micro-Raman Spectroscopy, a Powerful Technique Allowing Sure Identification and Complete Characterization of Asbestiform Minerals. Applied Sciences, 9, 3092.

Schlenker, J.L., Pluth, J.J., and Smith, J.V. (1977) Dehydrated natural erionite with stacking faults of the offretite type. Acta Crystallographica Section B, 33, 3265–3268.

Smith, T.R., and Cole, J.W. (1996) Stratigraphic and petrological variation of the Mount Somers Volcanics Group, mid Canterbury, New Zealand. New Zealand Journal of Geology and Geophysics, 39, 445–460.

Staples, L.W., and Gard, J.A. (1959) The fibrous zeolite erionite; its occurrence, unit cell, and structure. Mineralogical magazine and journal of the Mineralogical Society, 32, 261–281.

Tappenden, V.E. (2003) Magmatic response to the evolving New Zealand Margin of Gondwana during the Mid-Late Cretaceous. Ph.D thesis, University of Canterbury, Christchurch, New Zealand.

Toby, B.H. (2001) EXPGUI, a graphical user interface for GSAS. Journal of Applied Crystallography, 34, 210–213.

Van der Meer, Q.H.A., Waight, T.E., Whitehouse, M.J., and Andersen, T. (2017) Age and petrogenetic constraints on the lower glassy ignimbrite of the Mount Somers Volcanic Group, New Zealand. New Zealand Journal of Geology and Geophysics, 60, 209–219.

Van Gosen, B.S., Blitz, T.A., Plumlee, G.S., Meeker, G.P., and Pierson, M.P. (2013) Geologic occurrences of erionite in the United States: an emerging national public health concern for respiratory disease. Environmental Geochemistry and Health, 35, 419–430.

Wang, T., Luo, S., Tompsett, G.A., Timko, M.T., Fan, W., and Auerbach, S.M. (2019) Critical Role of Tricyclic Bridges Including Neighboring Rings for Understanding Raman Spectra of Zeolites. Journal of the American Chemical Society, 141, 20318–20324.

WHO (1986) Asbestos and Other Natural Mineral Fibers. United Nations Environment Programme, International Labour Organisation, World Heath Organization, Geneva.

——— (1997) Determination of airborne fibre number concentrations : a recommended method, by phase-contrast optical microscopy (membrane filter method), 53 p. World Health Organization.

Wylie, A.G. (2017) Asbestos and Fibrous Erionite. In J.R. Testa, Ed., Asbestos and Mesothelioma pp. 11–41. Springer International Publishing, Cham.

Figure captions

Figure 1. (a) Geological Map of Mount Somers Area; (b) Map of the South Island of New Zealand, indicating the Gawler Downs study area; (c) Geological Map of Gawler Downs, with sampling point.

Figure 2. (a) Overview of the road cutting where sampling took place; (b) image of the GD4a vesicle filled with fibrous erionite.

Figure 3. Results of the thermal analysis of sample GD4a up to 900 °C. (a) thermogravimetric analysis (TGA) and its first derivative (DTG); (b) analysis of the gases evolved during thermal reactions (MSEGA) measured using a quadrupole mass spectrometer.

Figure 4. FEG-SEM images of the GD4a erionite sample showing the asbestiform crystal habit. (a) low magnification picture; (b) zoom high magnification image of the previous fiber bundle.

842 **Figure 5**. Histograms of the measured fiber sizes for GD4a. (a) fiber length (L_f); (b) fiber width
843 (W_f); (c) fibril length (L_r); (d) fibril width (W_r).
844
845 **Figure 6**. TEM study of the GD4a erionite sample. (a) Fiber bundles; (b) high resolution image
846 of an erionite fiber; (c) the iron-rich smectite colloidal flakes laying on some erionite fibers; (d)
847 the *hhl* and *h*0*l* reconstruction planes of the 3DED data sets of erionite crystals.
848
849 **Figure 7**. Selected regions of the patterns with the observed data points (red), calculated points
850 (green), markers of the erionite reflections, and difference curve (magenta). (a) lab source; (b)
851 synchrotron source.
852
853 **Figure 8.** Representation of the 12–fold coordination environment of K^+ inside the cancrinite
854 cage. (a) when the value of the 6 K1—O2 distances is close to the value of the 6 K1—O3
855 distances, like in GD4a erionite, the coordination sphere is more symmetrical, resembling a
856 spherical shape; (b) when the value of the 6 K1—O2 distances departs from to the value of the 6
857 K1—O3 distances, like in other erionite structure models (e.g. Giacobbe et al. 2023), the
858 coordination gets closer to a hexagonal prism with two layers of oxygen atoms at more or less
859 the same height along the c axis.
860
861 **Figure 9**. (a) compositional diagram showing the extraframework cation content of erionite and
862 offretite samples from the literature (Alberti et al. 1997; Passaglia et al. 1998; Ballirano et al.
863 2009; Cametti et al. 2013; Gualtieri et al. 2016; Quiroz-Estrada et al. 2020; Battiston et al. 2022;

Giacobbe et al. 2023; Mattioli et al. 2023). Legend: black triangles = erionite; black circles = offretite; black cross = Gawler Downs (New Zealand), this work; (b) plot derived from the same literature data plotted in (a) with sample discrimination based on the calculated ratio Mg/(Ca+Na+K). Legend: erionites = white bars; offretites = black bars; GD4a sample from New Zealand = gray bar.

Figure 10. The best configuration around the Mg^{2+} in the erionite cavity showing a 6-fold coordination with 3 out of the 6 mutually exclusive H_2O molecules OW3 at 2.092 Å and 3 H_2O molecules OW7 at 1.897 Å.

Figure 11. Micro-Raman spectrum of erionite-K standard from Rome, Oregon (USA) (top), GD4a erionite sample (middle), and standard offretite from Saviore (Italy) (bottom). See text for details.

Figure 12. Comparison of the value of the Fiber Potential toxicity Index (FPTI) of GD4a erionite with those of other asbestiform erionites, a positive standard UICC crocidolite and a negative standard NYAD G wollastonite. The values are calculated using the online application available at *fibers-fpti.unimore.it/FPTI/* (Gualtieri et al. 2021). See the text for details.

TABLE 1. SEM Morphometric Analysis of GD4a fibers.

	Min	**Max**	**Mean**	**25th percentile**	**75th percentile**
L_f (μm)	50.71	307.96	210.47	111.25	248.33
W_f (μm)	2.70	29.93	12.07	6.02	18.10
L_f/W_f	3.95	99.34	25.40	9.89	33.31
L_r (μm)	50.71	307.96	206.82	111.25	243.93
W_r (μm)	0.34	3.15	1.36	1.03	1.61
$W_{r,TEM}$ (μm)	0.12	1.50	0.39		
L_r/W_r	25.10	717.44	171.05	99.33	212.25

Legend: L_f (fiber length); W_f (fiber width); L_r (fibril length); W_r (fibril width); $W_{r,TEM}$ (fibril width as determined from high resolution TEM data); L_f/W_f (aspect ratio for fiber); L_r/W_r (aspect ratio for fibril).

TABLE 2. Relevant bond distances (Å) calculated from the Rietveld refinement of the GD4a erionite sample.

Framework			
*T*1—O1	1.6290(6)		
*T*1—O2	1.5990(7)		
*T*1—O3	1.6941(6)		
*T*1—O4	1.6283(8)		
Mean	1.6376		
*T*2—O1×2	1.6475(8)		
*T*2—O5	1.6759 (7)		
*T*2—O6	1.6154(7)		
Mean	1.646575		
Extraframework			
Ca1—OW1×2	2.9793(10)	K1—O2×6	3.1539(11)
Ca1—OW1	2.9792(10)	K1—O3×6	3.1601(11)
Ca1—OW2×3	2.4435(9)		
Ca1—OW6×2	2.5054(10)	K2—O1×4	3.2246(11)
Ca1—OW6	2.5055(10)	K2—O4×2	3.1283(11)
		K2—OW1×4	3.3840(12)
Na1—OW2×3	2.4435(9)	K2—OW3×4	3.0109(11)
Na1—OW6×2	2.5054(10)		
Na1—OW6	2.5055(10)	K3—O5×3	3.1059(13)
		K3—O6×3	3.5174(13)
Ca2—OW2×2	2.4276(9)	K3—OW3×6	3.1010(13)
Ca2—OW2	2.4275(11)		
Ca2—OW3×6	2.6542(12)	Mg1—OW3×6	2.092(1)
Ca2—OW6×2	2.6524(10)	Mg1—OW5×3	2.423(1)
Ca2—OW6	2.6525(10)	Mg1—OW7×3	1.897(1)
Ba2—OW3×6	2.6542(12)		

Ba2—OW6	3.0287(10)
Ba2—OW6×2	3.0286(10)
Ba2—OW6×2	2.6524(10)
Ba2—OW6	2.6525(10)

Figure 1

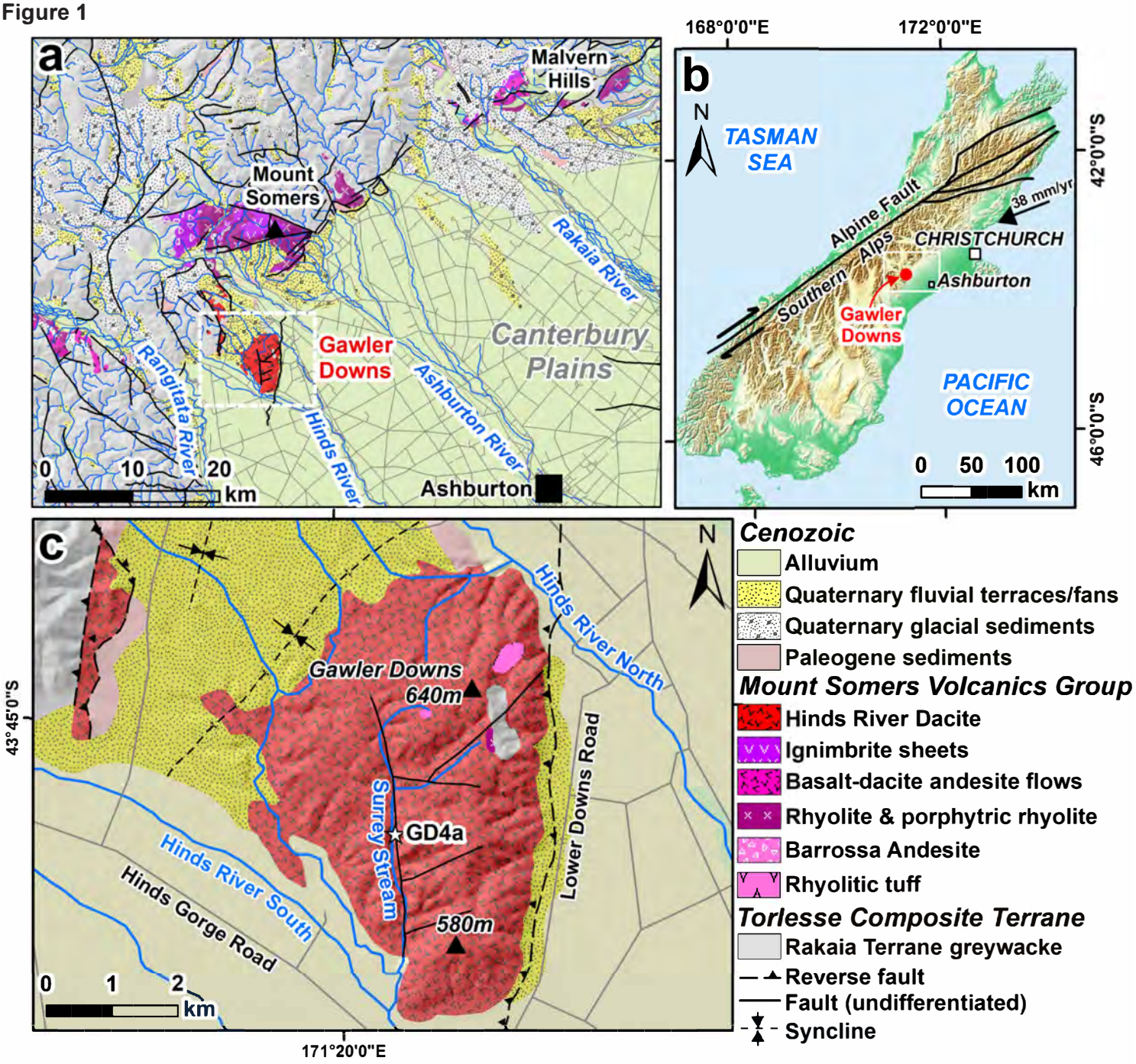
a
Malvern Hills
Mount Somers
Rakaia River
Gawler Downs
Canterbury Plains
Rangitata River
Ashburton River
Hinds River
Ashburton
0 10 20 km
b
168°0'0"E
172°0'0"E
42°0'0"S
46°0'0"S
N
TASMAN SEA
Alpine Fault
38 mm/yr
CHRISTCHURCH
Southern Alps
Ashburton
Gawler Downs
PACIFIC OCEAN
0 50 100 km
c
N
Hinds River North
Gawler Downs
640m
Surrey Stream
GD4a
580m
Lower Downs Road
Hinds River South
Hinds Gorge Road
0 1 2 km
43°45'0"S
171°20'0"E
Cenozoic
Alluvium
Quaternary fluvial terraces/fans
Quaternary glacial sediments
Paleogene sediments
Mount Somers Volcanics Group
Hinds River Dacite
Ignimbrite sheets
Basalt-dacite andesite flows
Rhyolite & porphytric rhyolite
Barrossa Andesite
Rhyolitic tuff
Torlesse Composite Terrane
Rakaia Terrane greywacke
Reverse fault
Fault (undifferentiated)
Syncline

Figure 2

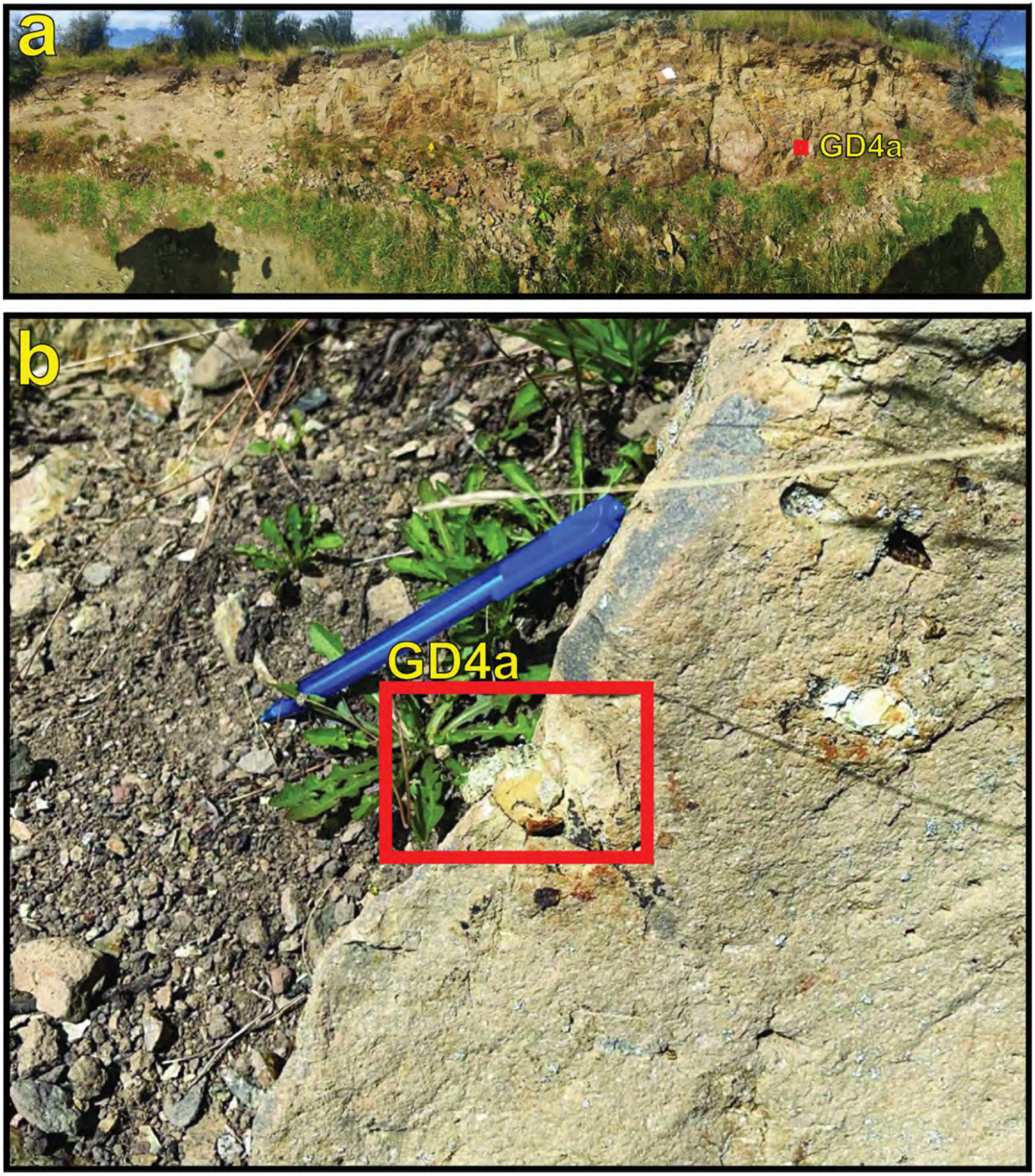

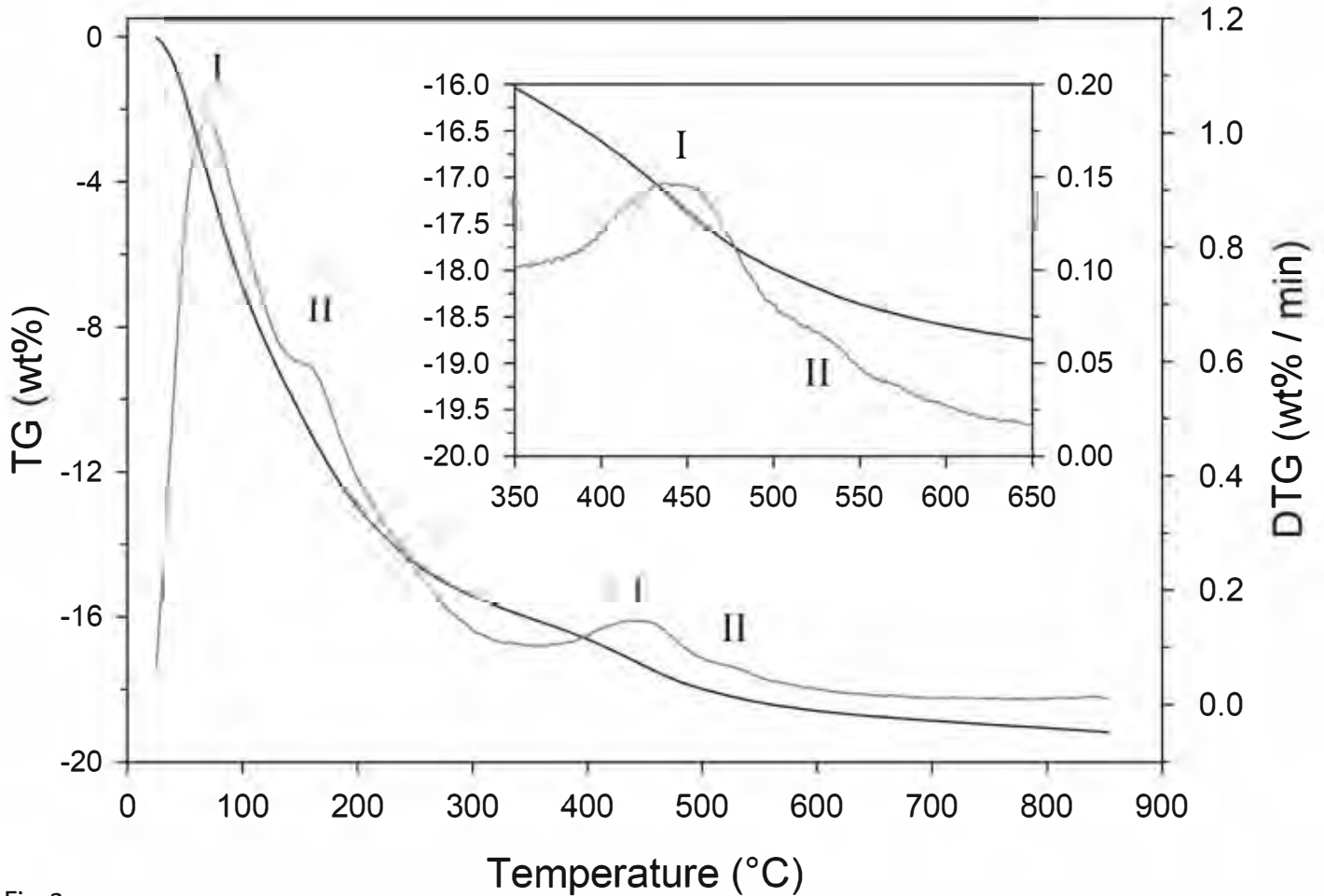
TG (wt%)
DTG (wt% / min)
Temperature (°C)
0
-4
-8
-12
-16
-20
1.2
1.0
0.8
0.6
0.4
0.2
0.0
0
100
200
300
400
500
600
700
800
900
I
II
-16.0
-16.5
-17.0
-17.5
-18.0
-18.5
-19.0
-19.5
-20.0
0.20
0.15
0.10
0.05
0.00
350
400
450
500
550
600
650

Fig. 3a

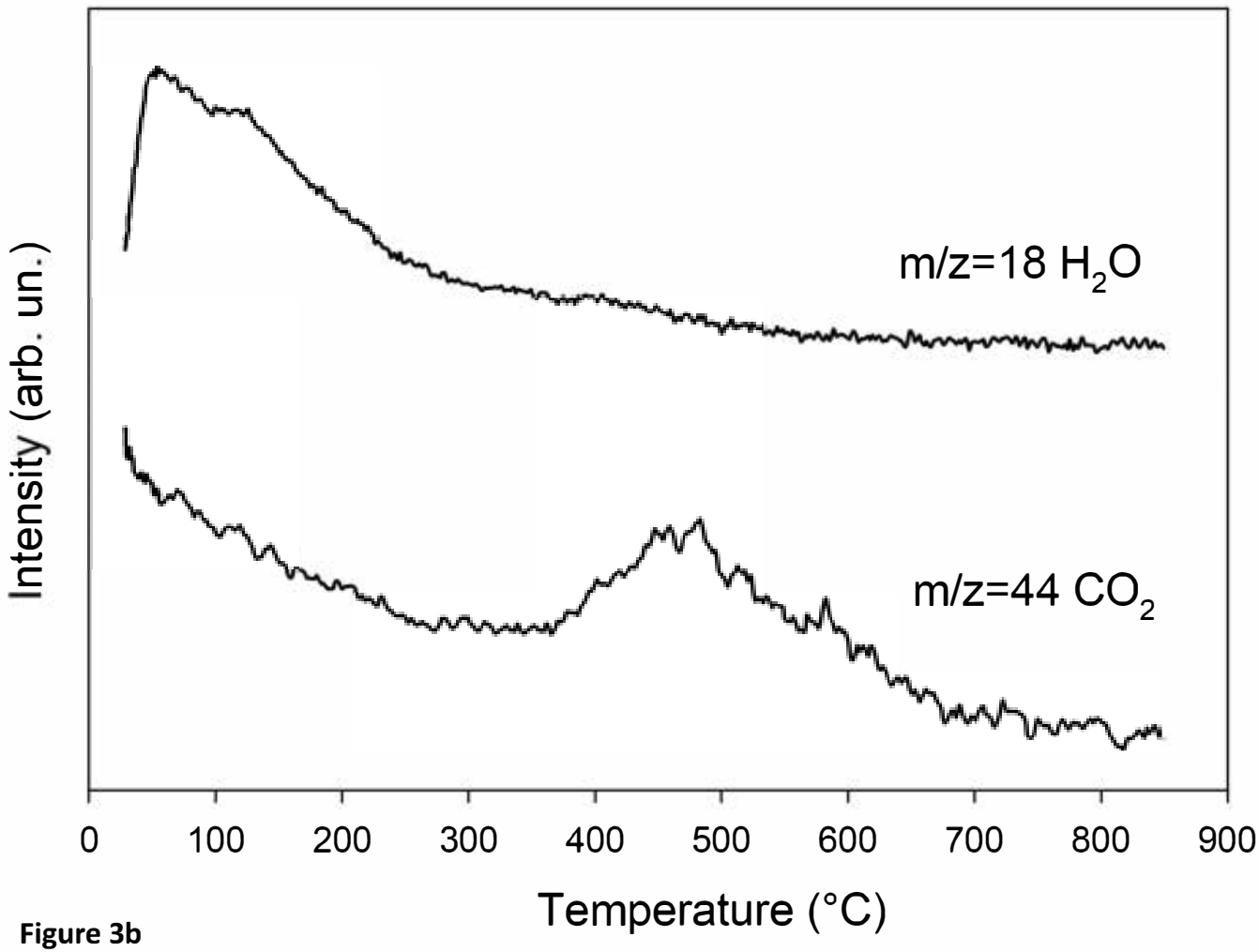
Intensity (arb. un.)
m/z=18 H2O
m/z=44 CO2
0
100
200
300
400
500
600
700
800
900
Temperature (°C)

Figure 3b

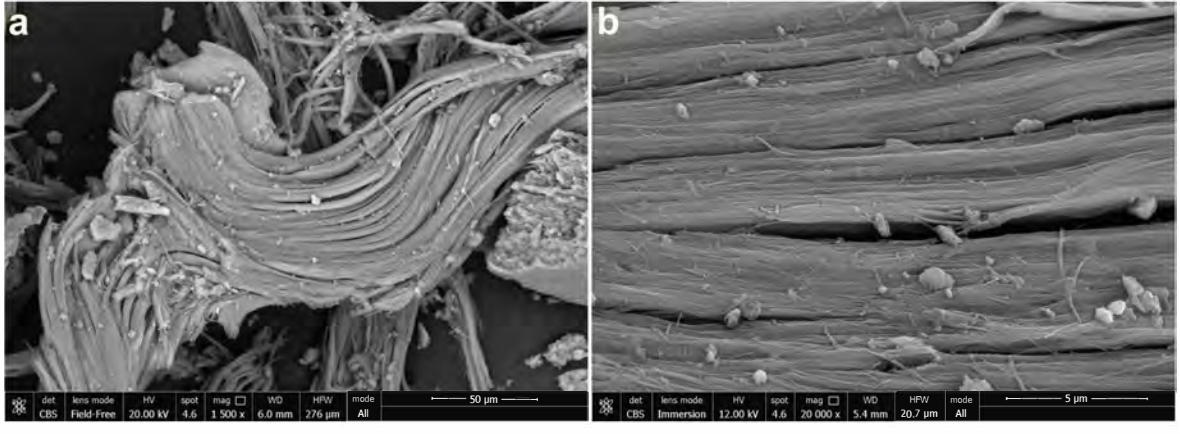
a
det CBS
lens mode Field-Free
HV 20.00 kV
spot 4.6
mag 1 500 x
WD 6.0 mm
HFW 276 µm
mode All
50 µm
b
det CBS
lens mode Immersion
HV 12.00 kV
spot 4.6
mag 20 000 x
WD 5.4 mm
HFW 20.7 µm
mode All
5 µm

Figure 4

Figure 5

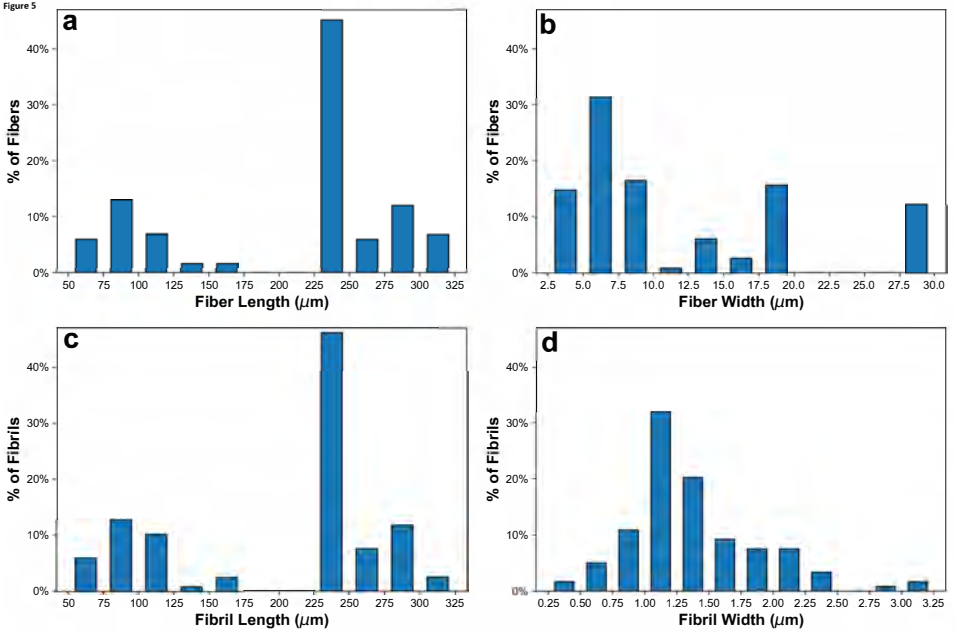
a
% of Fibers
40%
30%
20%
10%
0%
50 75 100 125 150 175 200 225 250 275 300 325
Fiber Length (μm)
b
% of Fibers
40%
30%
20%
10%
0%
2.5 5.0 7.5 10.0 12.5 15.0 17.5 20.0 22.5 25.0 27.5 30.0
Fiber Width (μm)
c
% of Fibrils
40%
30%
20%
10%
0%
50 75 100 125 150 175 200 225 250 275 300 325
Fibril Length (μm)
d
% of Fibrils
40%
30%
20%
10%
0%
0.25 0.50 0.75 1.00 1.25 1.50 1.75 2.00 2.25 2.50 2.75 3.00 3.25
Fibril Width (μm)

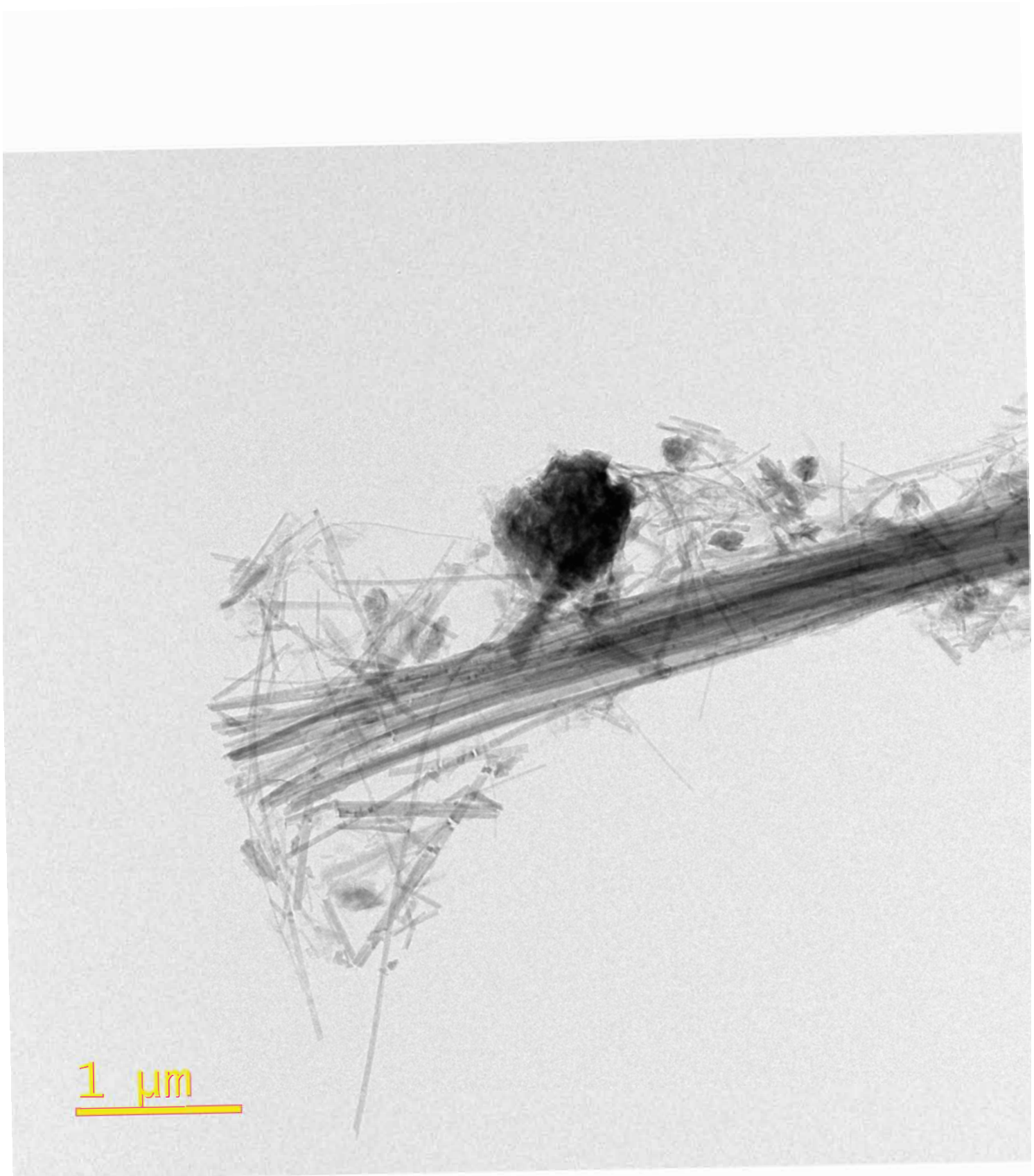

Fig. 6a

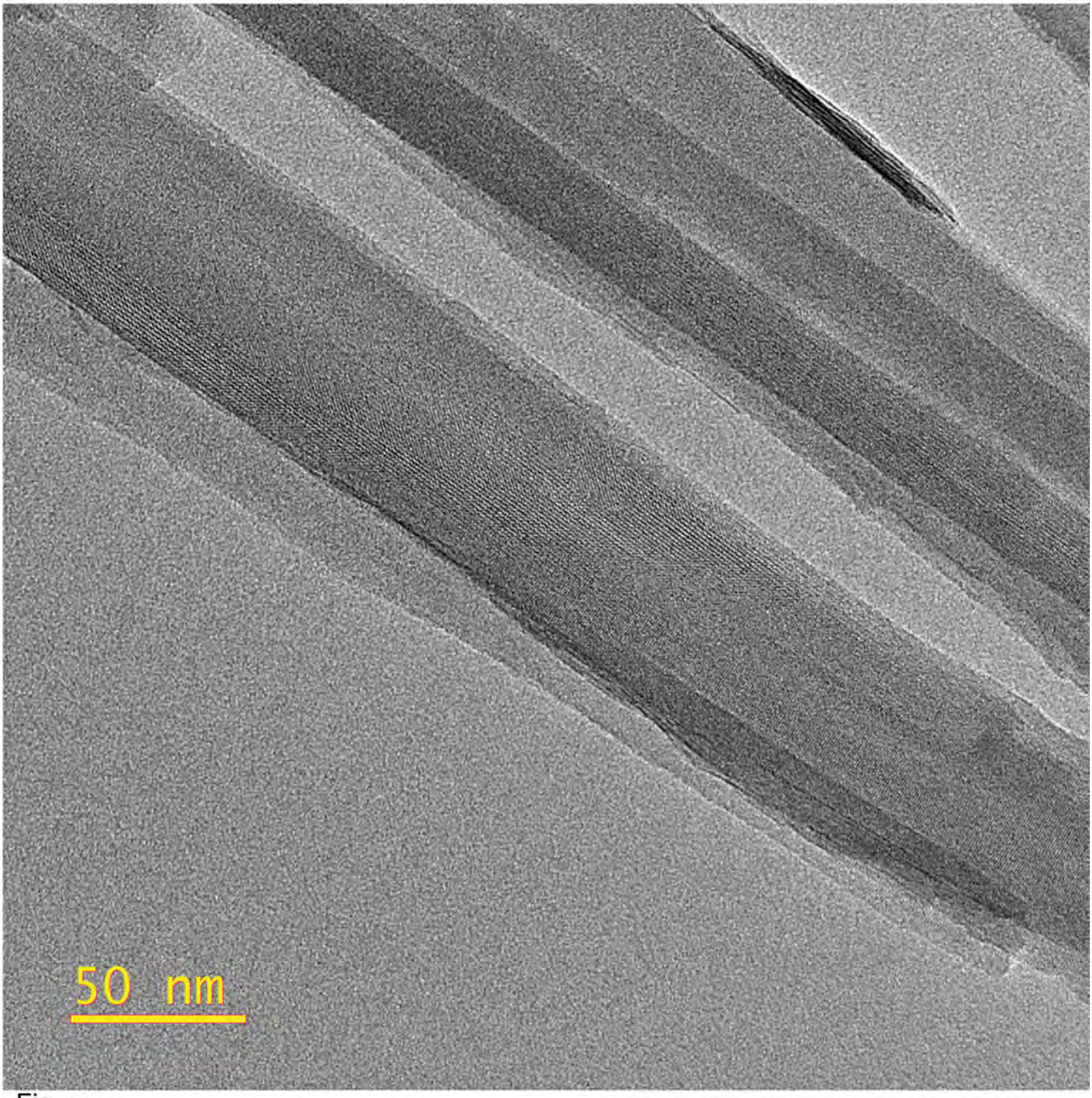

Fig. 6b

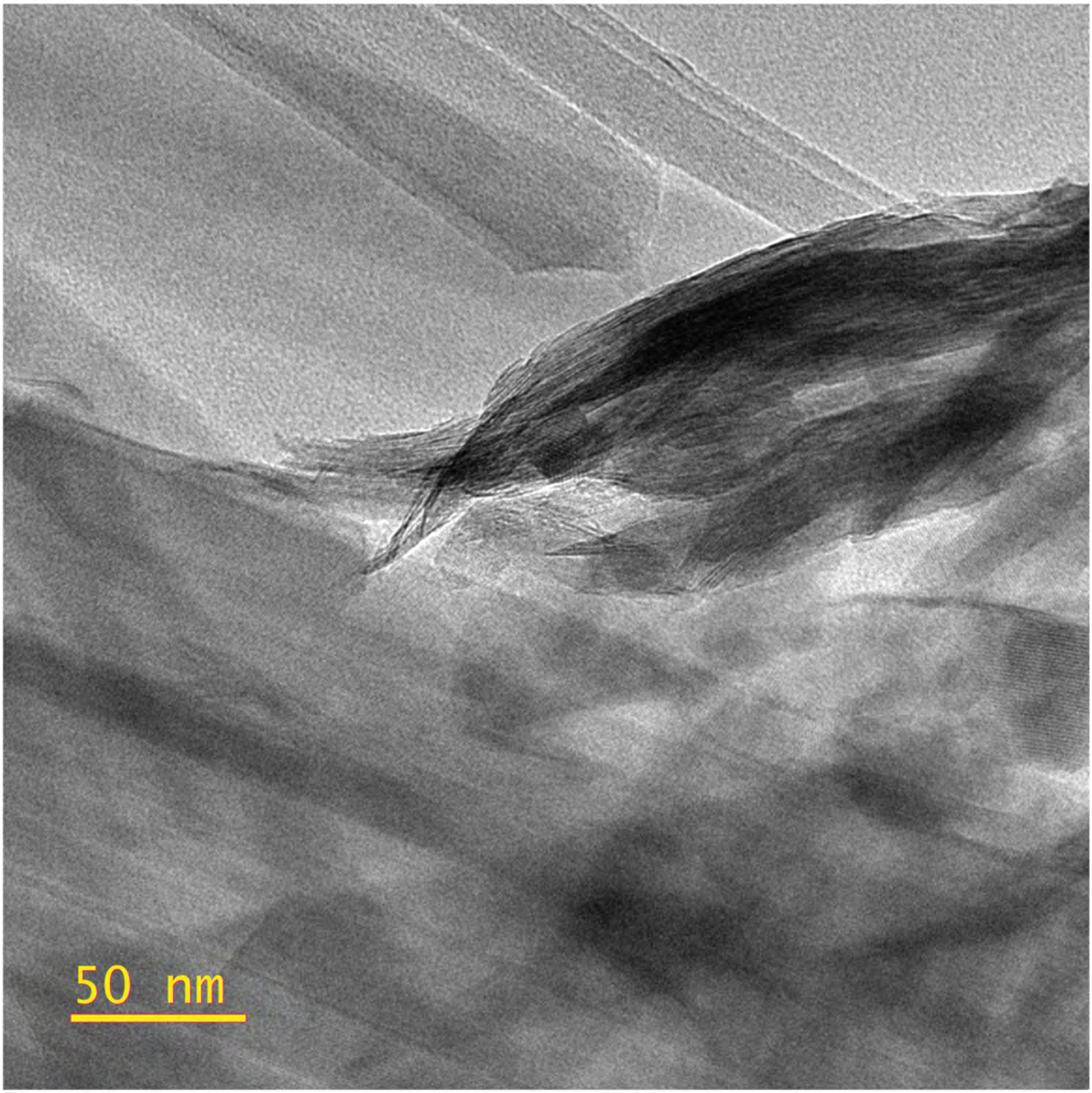

Fig 6c

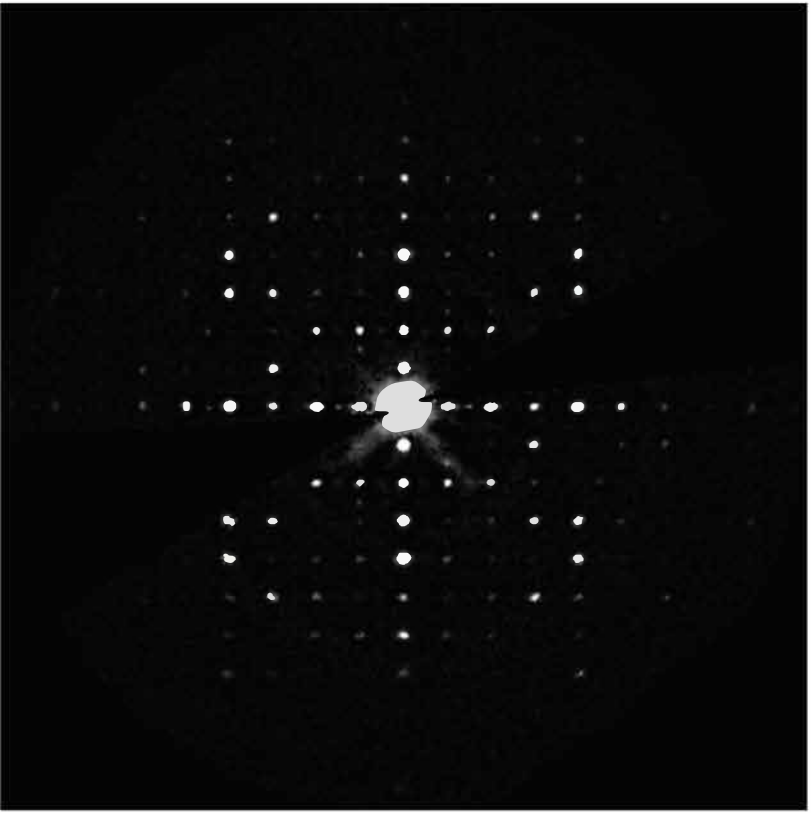

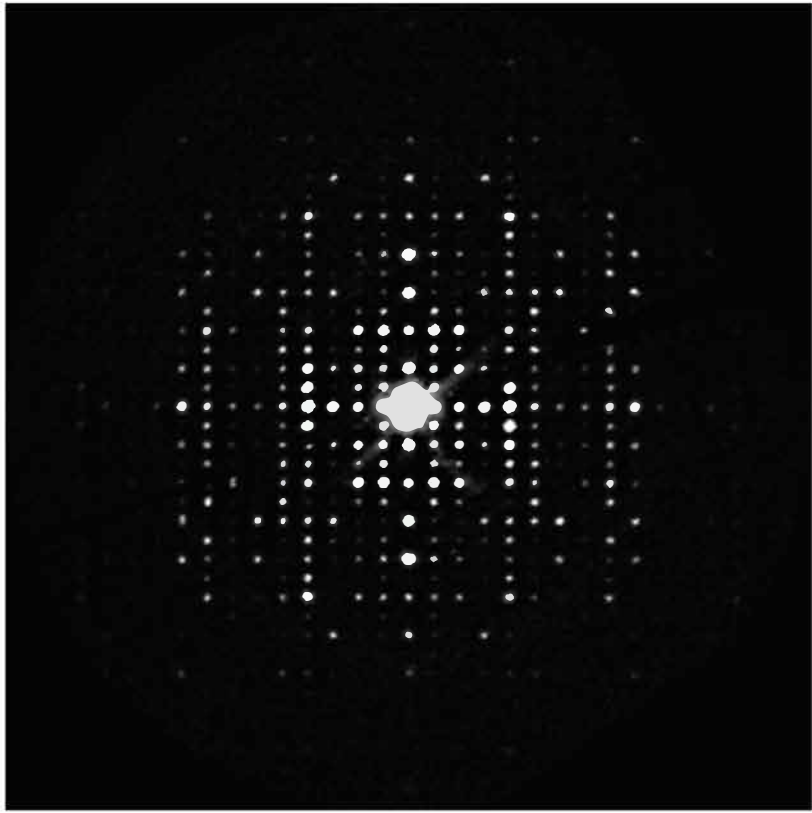

hhl ***h0l***

Fig **6d**

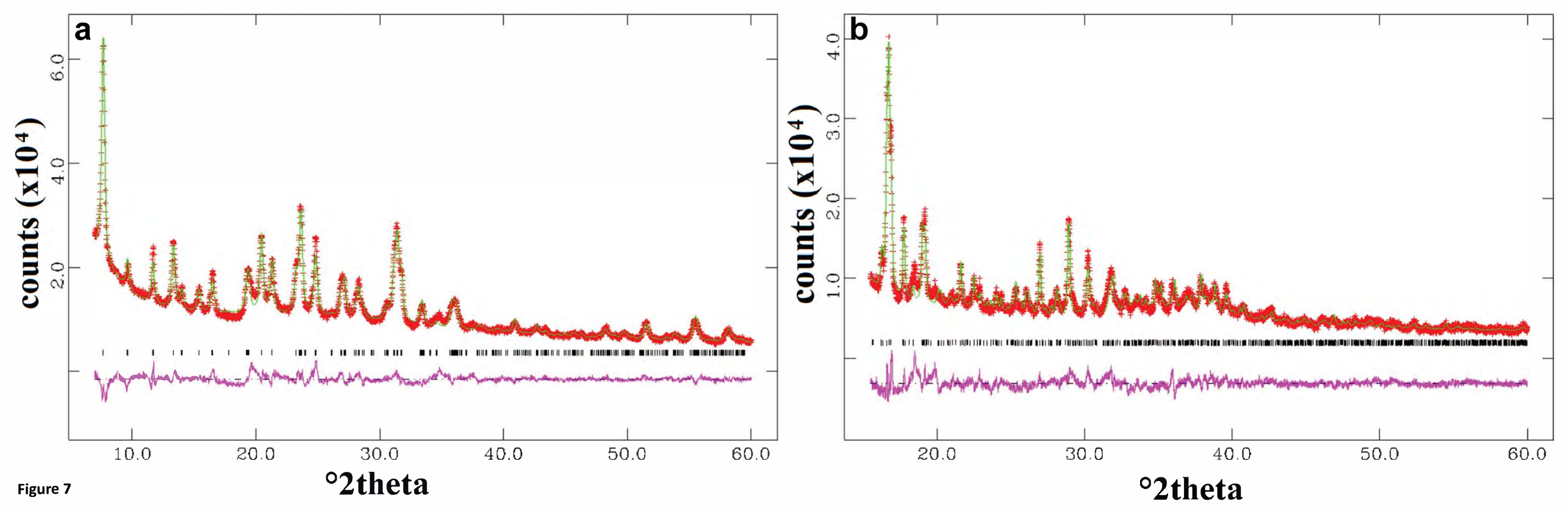
a
counts (x10⁴)
6.0
4.0
2.0
10.0
20.0
30.0
40.0
50.0
60.0
°2theta
b
counts (x10⁴)
4.0
3.0
2.0
1.0
20.0
30.0
40.0
50.0
60.0
°2theta

Figure 7

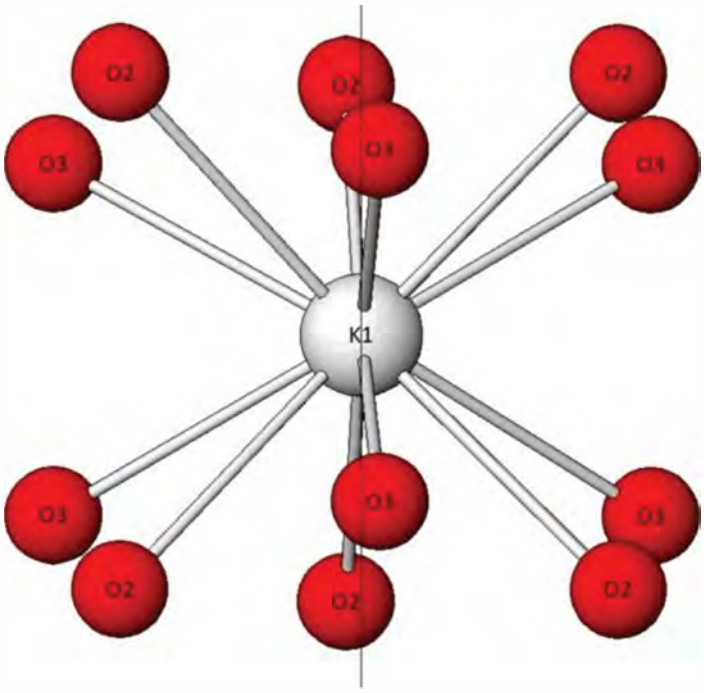

a

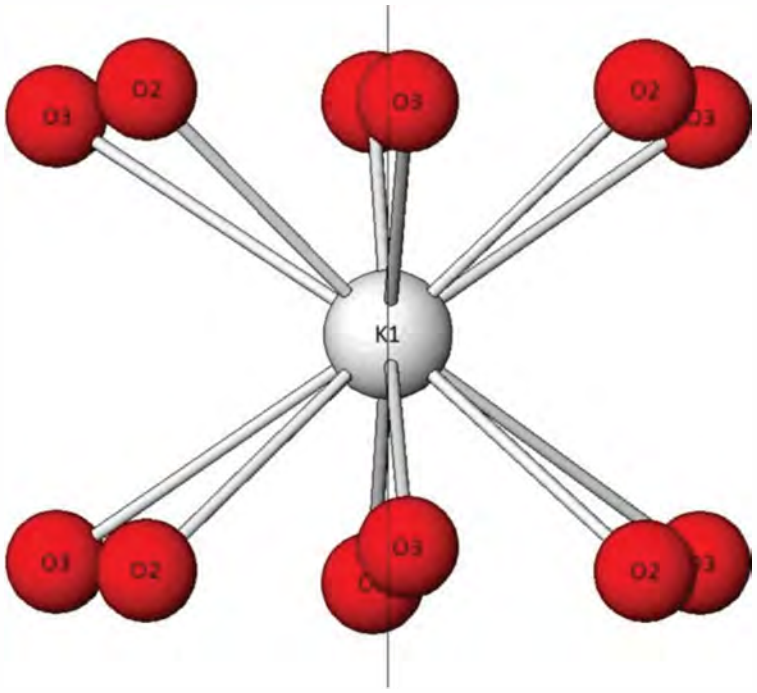

b

Figure **8**

Figure 9a

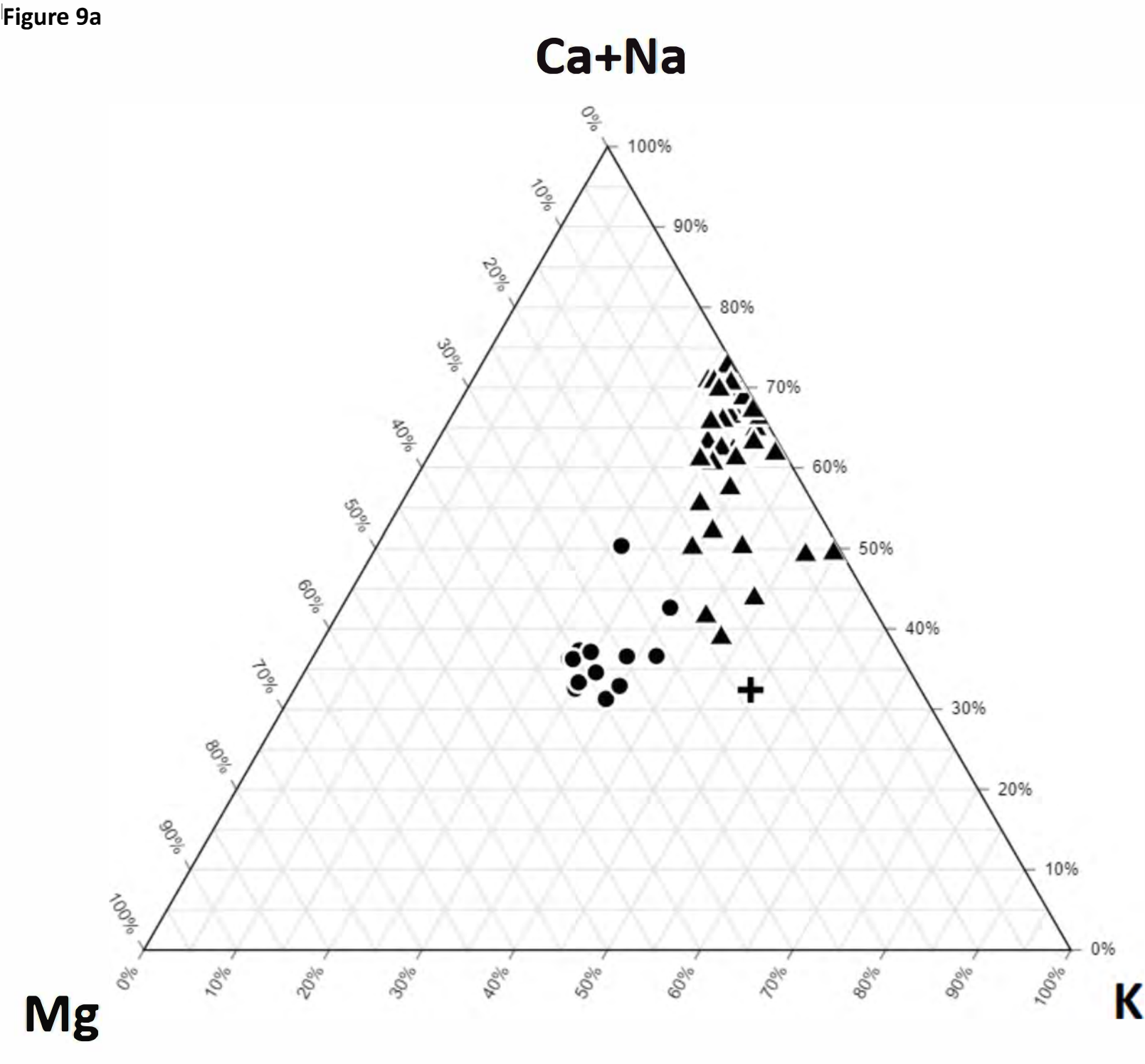

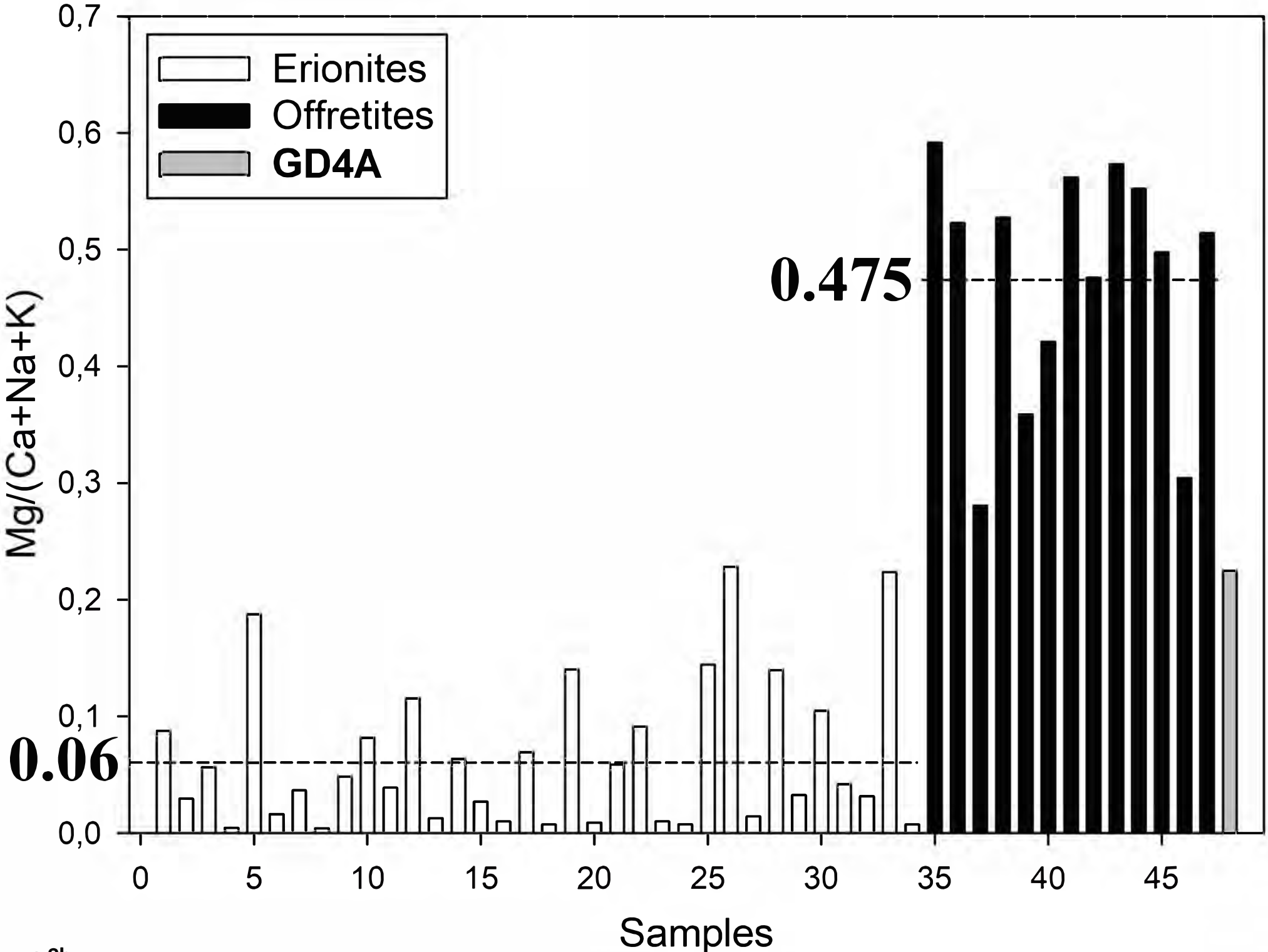
Erionites
Offretites
GD4A
0.475
0.06
Mg/(Ca+Na+K)
Samples
0,0
0,1
0,2
0,3
0,4
0,5
0,6
0,7
0
5
10
15
20
25
30
35
40
45

Figure 9b

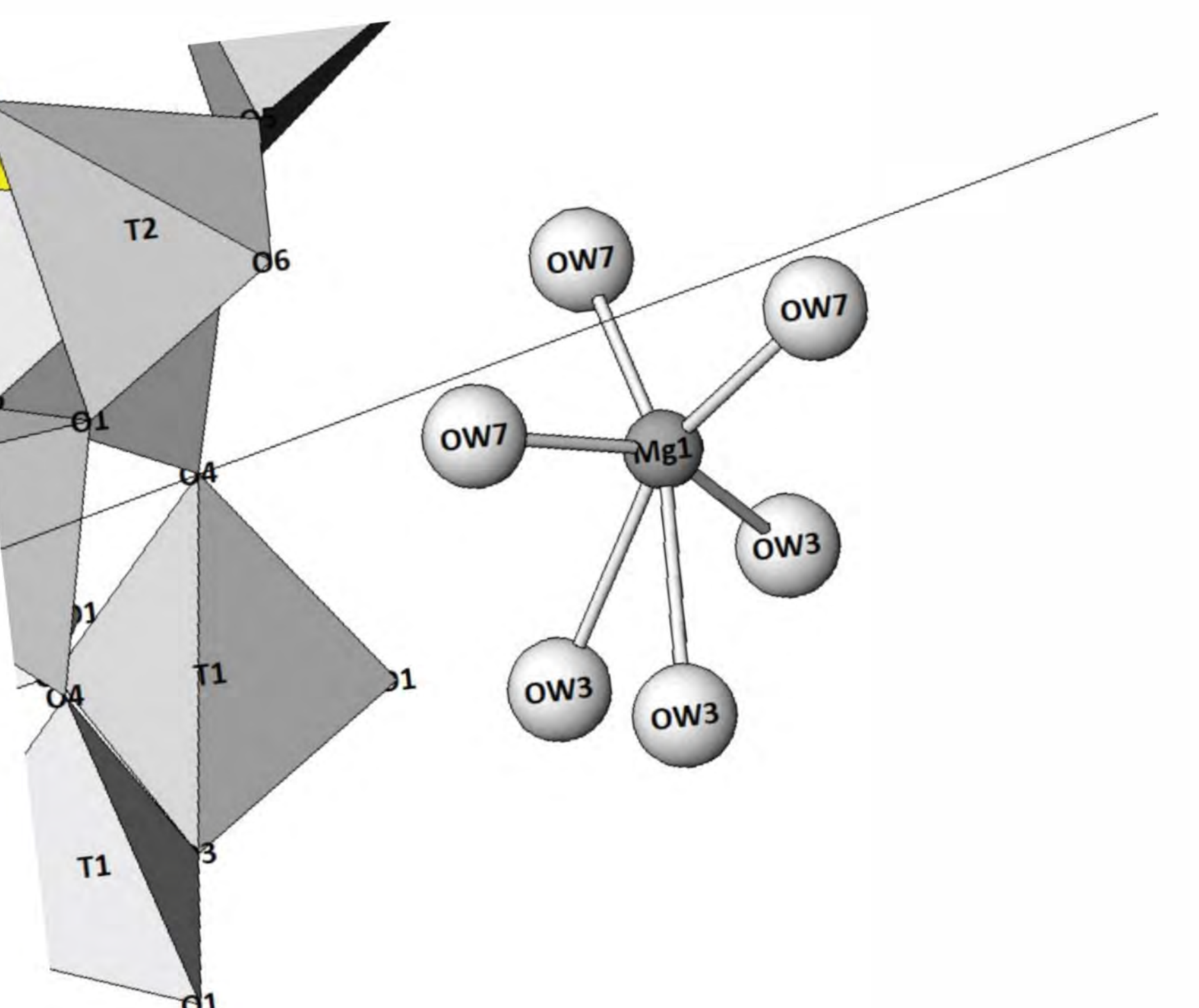
T2
O6
O1
O4
T1
T1
OW7
OW7
OW7
Mg1
OW3
OW3
OW3

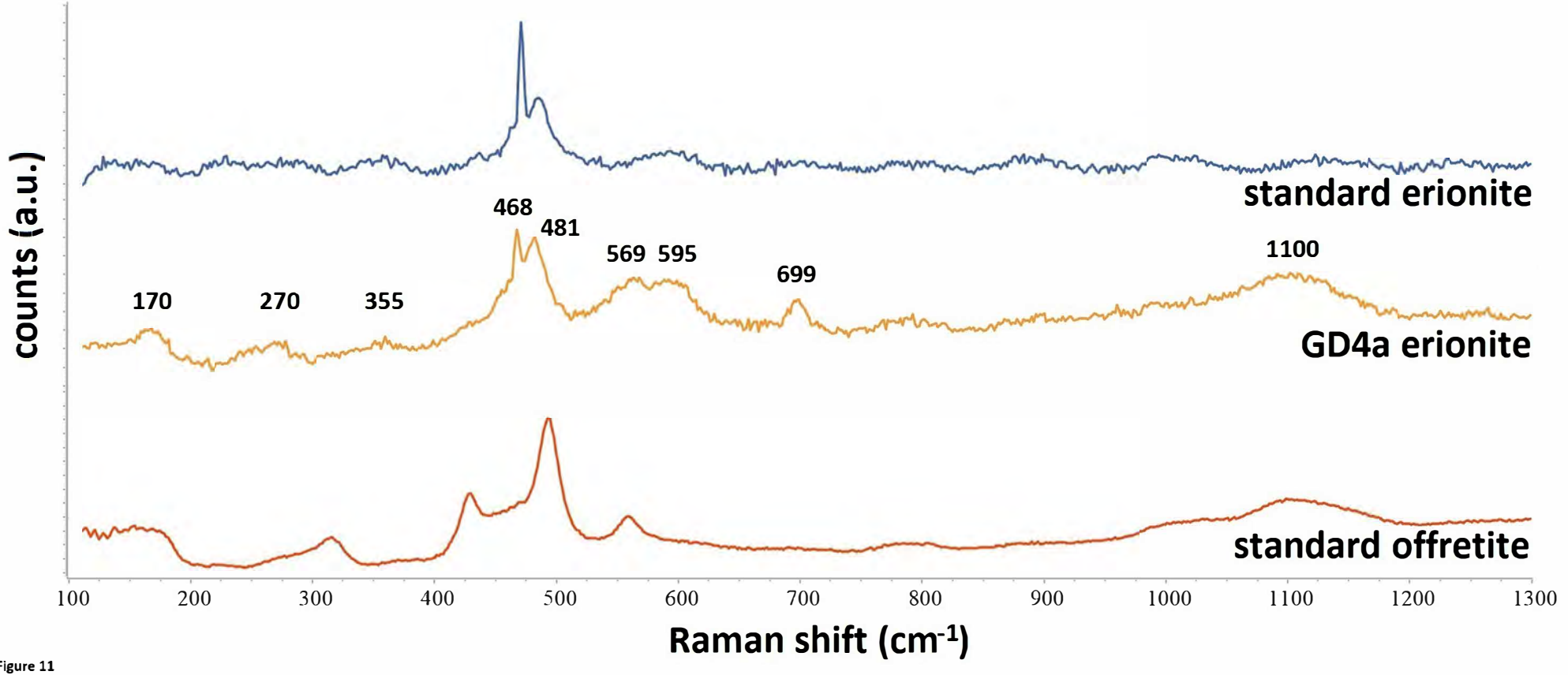
counts (a.u.)
standard erionite
468
481
569
595
699
1100
170
270
355
GD4a erionite
standard offretite
100
200
300
400
500
600
700
800
900
1000
1100
1200
1300
Raman shift (cm-1)

Figure 11

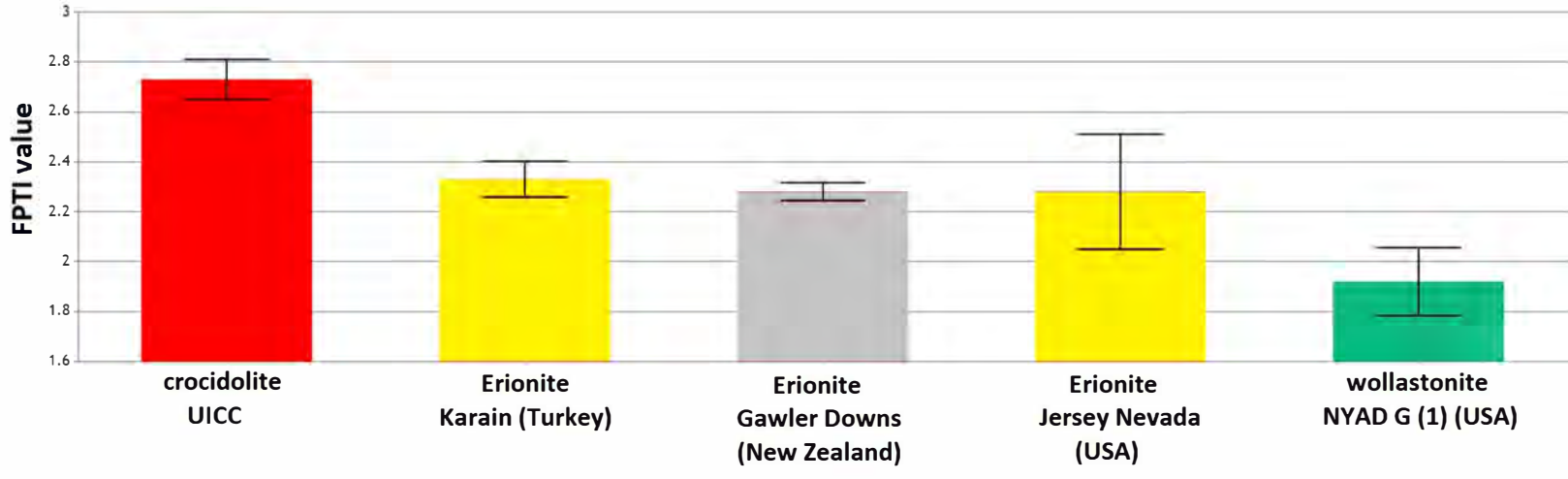
FPTI value
3
2.8
2.6
2.4
2.2
2
1.8
1.6
crocidolite
UICC
Erionite
Karain (Turkey)
Erionite
Gawler Downs
(New Zealand)
Erionite
Jersey Nevada
(USA)
wollastonite
NYAD G (1) (USA)

Figure 12